Deployment dynamics of a high strain deployable rolled-up composite SAR antenna

Original
Deployment dynamics of a high strain deployable rolled-up composite SAR antenna / Tresoldi, A., Shore, J., Pagani, A., Aglietti, G.. - In: INTERNATIONAL JOURNAL OF SOLIDS AND STRUCTURES. - ISSN 0020-7683. - STAMPA. - 310:(2025). [10.1016/j.ijsolstr.2024.113208]

Publisher:
Elsevier

Published
DOI:10.1016/j.ijsolstr.2024.113208

International Journal of Solids and Structures 310 (2025) 113208

Contents lists available at ScienceDirect

International Journal of Solids and Structures

journal homepage: www.elsevier.com/locate/ijsolstr

Deployment dynamics of a high strain deployable rolled-up composite SAR antenna

Annalisa Tresoldi [a,*], Jason Shore [a], Alfonso Pagani [b], Guglielmo Aglietti [a]

[a] *Te Pūnaha Ātea - Space Institute, University of Auckland, 20 Symond Street, 1010, Auckland, New Zealand*
[b] *MUL2 Lab, Department of Mechanical and Aerospace Engineering, Politecnico di Torino, Corso Duca degli Abruzzi, 24, Torino, 10129, Italy*

ARTICLE INFO

Keywords:
Deployment dynamics
Lagrangian
High strain composite
Synthetic Aperture Radar

ABSTRACT

The Deployable Rolled-up Composite Antenna - Synthetic Aperture Radar (DERCA-SAR) concept design is proposed for a 12U CubeSat low-power remote sensing application. A SAR reflectarray system is considered to be implemented on a High-Strain Composite (HSC) structure with a shallow "tape-measure" inspired shape. The stiffness required in the deployed state is provided by the cross-sectional curvature of the shell, which will be rigidly maintained at the root during stowage. To provide a low-mass solution for this application, the DERCA-SAR technology considers flattening and coiling the shell tip until it reaches the clamped root and deploys by releasing the elastic strain energy stored in the coiled configuration. In this paper, two analytical models are developed to describe the deployment dynamics of this structure and predict the deployment velocity that may impact the antenna performance. Given an initial coil radius r, which is much smaller than the natural radius R to fit a nanosatellite platform, the deployment occurs in two stages that have been revealed through experiments. The first blossoming phase is described as an expanding and uncoiling process based on the Lagrangian approach. The second and more chaotic phase of the deployment is modelled using a Hencky-type model that discretises the shell's structure in a multi-pendulum system connected by elastic rotational hinges/springs. In this model, the shell's stiffness is made to locally change based on the characteristic tape springs' moment–rotation relationship and the implementation of a stiffness function. The analytical results are then compared to experimental data derived from deployment testing on samples of the shells with different material properties. The predictions from the two models capture the significant trends of the data well, and predict the maximum speed with an error of $< 10\,\%$.

1. Introduction

In recent years, CubeSats have provided a short development time and cost-efficient solution for some EO missions, unlocking a new era of small and nano spaceborne radar technologies (Xue et al., 2008; Peral et al., 2018). Thanks to the miniaturisation of the electronic components and their reduced power consumption, Synthetic Aperture Radar (SAR) payloads have been increasingly implemented on small satellites (Filippazzo and Dinand, 2017). SAR systems enable high-resolution imaging of the Earth's surface and provide local/global coverage on areas often impenetrable to visible and infrared remote sensing techniques (Birk et al., 1995). Such capabilities can be further exploited by increasing the revisit time and number of observations through developing SAR constellations implemented in CubeSats. However, because SAR systems' performance metrics, such as resolution, sensitivity, and image quality, are proportional to the antenna size (Kim and Jordan, 2006), the structure that supports the antenna is a critical design aspect that impacts the final mass and volume of the satellite. To counter the volume constraints and limited resources available, most small platforms require deployable subsystems to install large payloads and provide a high stowage efficiency during launch and nominal performance in the operational phase (Aglietti et al., 2020).

Generally, SAR antennas have been implemented on deployable active (Akbar et al., 2016) or reflective (Huang, 2007) planar array systems, large parabolic reflectors (Barrett et al., 2007), and more recently, on deployable thin-film membranes (Zhi-Quan et al., 2017) inspired by gossamer structures (Fernandez et al., 2014) and solar sail architectures (Seefeldt et al., 2014). Although each technology shows points of strength in satisfying CubeSat requirements (Chahat et al., 2019), installing a SAR system is not only driven by the mass and volume constraints imposed by a small platform. The mission's specifications and the target application are important factors that impact the SAR system requirements and, in turn, the trade-off on the structural design.

---

* Corresponding author.
E-mail address: atre682@aucklanduni.ac.nz (A. Tresoldi).

https://doi.org/10.1016/j.ijsolstr.2024.113208
Received 31 August 2024; Received in revised form 15 December 2024; Accepted 23 December 2024

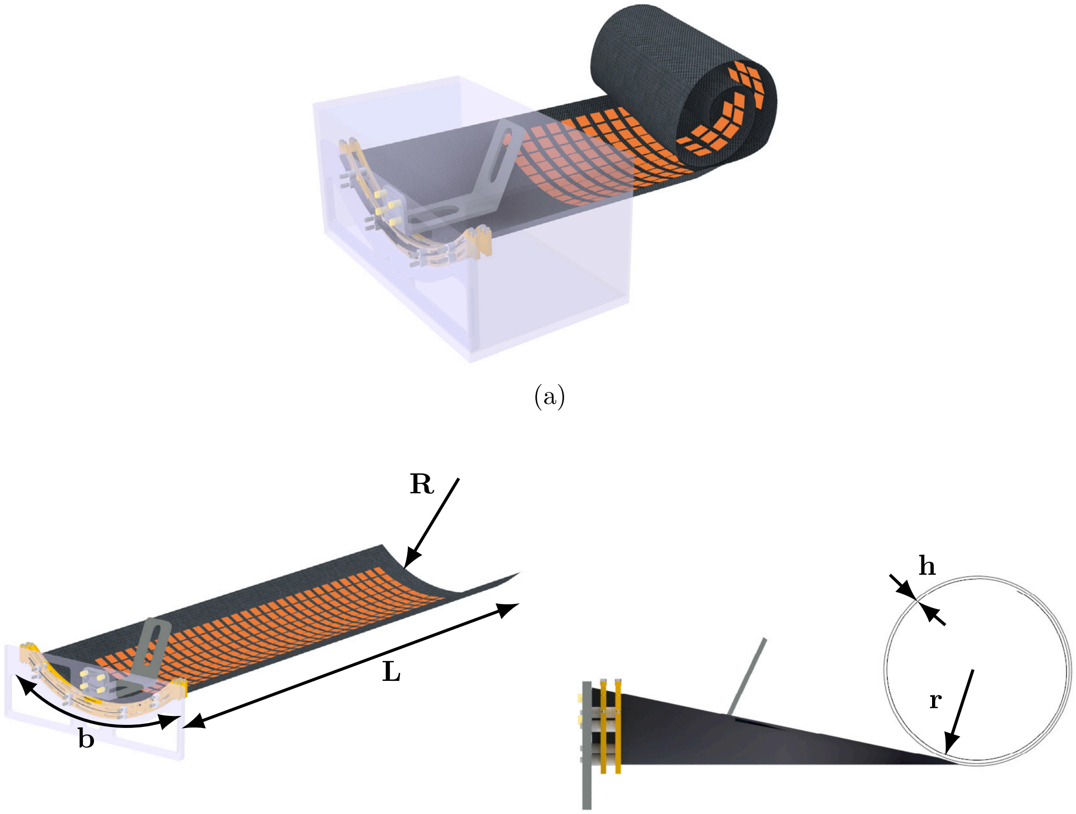

(a)

(b)

(c)

Fig. 1. CAD model of the DERCA-SAR technology in a partially deployed (a), fully deployed (b) and coiled state (c) with the HSC's geometric features.

The SAR concept design presented in this work is tailored for a 12U nanosatellite low-power maritime surveillance application and consists of a single and self-supporting antenna structure shaped like a shallow tape spring, as shown in Fig. 1(b). Such a structure is a High-Strain Composite (HSC) shell that trades off the structural stiffness, mechanical complexity and high stowage efficiency required for this application.

HSC booms, tape springs (Wang et al., 2019; Pagani et al., 2023) and STEMs (Rimrott and Fritzsche, 2000) are commonly used in space applications as a secondary system that enables and assists the stowage and the deployment of large instrumentation installed on small satellites (Fernandez, 2017). In this paper, a HSC shell with a slightly curved cross-section is considered the primary structure for a DEployable Rolled-up Composite Antenna (DERCA) that operates as the substrate for a reflectarray system. Thanks to its adaptive shape and self-extensible capability, a HSC structure can be stored in a highly elastically deformed configuration and then released to its naturally curved rigid state. A partially deployed configuration of the DERCA-SAR technology is shown in Fig. 1(a).

A characteristic feature of this design can be seen in Fig. 1, in which the natural curvature of the shell is maintained at the root to stiffen the deployed state using a clamped boundary condition. A clamped root is used in Roccor's COBRA system that utilises a curved HSC beam to support and roll out a solar array technology (Turse et al., 2019). Differently from the COBRA's system, in which the beam is coiled around the clamped beam's root, the DERCA-SAR technology considers flattening and coiling the shell tip until it reaches the clamped root on a deployment drum, which is then removed, as described in Tresoldi et al. (2023a). To provide a low-mass solution for this application, active motors are avoided, and the deployment is driven by the elastic strain energy stored in the coiled configuration. The coiled shell is guided outward by an angled deployment plate. A similar HSC boom's utilisation is the ROC-FALL De-orbit Device, where the HSC's design enables the deployment of a rectangular sail through a smooth release of strain energy (Davis et al., 2019).

Generally, the process and stages of the deployment of coiled booms have been investigated to assess the deployment stability (Yeong-Bae et al., 2023) and understand the structural dynamics of these structures while returning to their original shape (Seffen and Pellegrino, 1999). Based on the deployer configuration and the deployment actuator, analytical models have been developed and validated against experimental tests to describe HSC booms' deployment dynamics. In the case of self-deployment, one relevant aspect that has been investigated is the impact that surface deformations caused by material relaxation have on the HSC performance. In fact, due to long-term stowage (Brinkmeyer et al., 2015), viscoelastic surface distortions may occur after the unrolling process, which lowers the boom's efficiency or can damage the electronics that are installed or connected to it. In Okuizumi et al. (2014), a one-dimensional spring-mass system is proposed to predict the deformation and motion of a rollable boom designed to support the deployment of membrane structures. Another critical aspect that has been studied is the deployment velocity, which, if is too high, can cause undesired disturbances to the Attitude and Orbit Control System (AOCS), damage the HSC structure and impart a damaging shock to the satellite. In most deployment dynamics models described in the literature, the deployment velocity is derived by considering a coil radius r that is equal to the natural radius R. In addition, most of the analytical models account for a structure that unrolls on a spool and elongates flat to recover the initial transverse curvature by returning to its minimum strain energy state. For example, in Seffen and Pellegrino (1999), a Lagrange approach is used to build the equations of motion for a coiled tape spring in which the initial coil radius is constant. The same assumption is adopted in Brinkmeyer et al. (2015), in which an analytical model, built on (Rimrott and Fritzsche, 2000), is presented for orthotropic materials to estimate the deployment force and velocity of stored tape springs. To derive the "ejection" velocity, the authors used an energy method in which the tape spring is assumed to uncoil at a radius that remains constant during the initial phase of the deployment before extending out. In the event that $r < R$, an unwinding phenomenon, known as "blossoming", may occur in coiled tape springs and booms (Wang et al., 2020b). Instead of uncoiling, such structures naturally expand before extending out of the container in which they are housed, increasing the radius of the coiling. This event can cause a deployment failure where the boom gets jammed in the deployer. A prediction of the tip force that coiled booms can withstand before blossoming has been derived by an energy model developed by Hoskin et al. for mono-stable isotropic materials (Hoskin et al., 2017) and further investigated by Sicong et al. for bistable composites (Wang et al., 2020a) and booms (Wang et al., 2024). In their models, blossoming is described in the case where a boom is coiled around a spool, and a system of compression rollers and springs maintains the coil tight while the spool rotates. This configuration shows that when the coil radius is equal to the natural radius, $r = R$, the blossoming effect is diminished compared to the case of $r < R$. Hence, blossoming can be neglected when this assumption is made.

In this study, blossoming plays a key role in the first phase of the DERCA deployment. In fact, driven by the necessity to increase the packaging efficiency of the system and fit a nanosatellite platform, the DERCA technology requires a tightly coiled structure with an initial coil radius r which is much smaller than R. Therefore, unlike previous models in the literature, blossoming is accounted for in this work and modelled when $r < R$. Given the occurrence of this initial expansion and due to the DERCA antenna's aspect ratio tailored for this application, the "unrolling carpet" process, which commonly characterises tape springs' deployment (Mao et al., 2017), is replaced by a combination of deployment stages that have been verified experimentally. In fact, the DERCA deployment can be split into two different stages, where the shell first expands and unrolls and then opens up completely. To evaluate the impact that the DERCA system may have on the satellite asset and on the antenna performance, DERCA deployment dynamics is presented through two analytical models that estimate the deployment velocity of the system at each deployment phase. First, based on the Lagrangian approach developed in Seffen and Pellegrino (1999), blossoming is modelled as an expanding and uncoiling process, where the tip speed is estimated for the DERCA system and different shell geometries. Secondly, the deployment tip speed after blossoming is estimated by developing a Hencky-type model that discretises the shell's structure in a multi-pendulum system (Wang et al., 2020c) connected by elastic rotational hinges/springs. Here, the characteristic tape springs' moment–rotation relationship and localised elastic folds that occur before straightening (Seffen and Pellegrino, 1999) are considered to model the stiffness-changing behaviour that the shell undergoes during this phase. In addition, experimental tests are also presented to validate the analytical models and compare the results. Finally, a Finite Element (FE) model of the deployment process is used to highlight the steps of the blossoming process to gain further insight.

2. Experimental setup and deployment

To understand the deployment dynamics of the DERCA structure (Tresoldi et al., 2023b), deployment testing was conducted to observe the shell's opening behaviour and evaluate the deployment velocity. The deployments were recorded in a motion camera testing room using three shells that were manufactured from plies with the material properties given in Table 1. The layups, which have been previously studied in Tresoldi et al. (2023b), are given in Table 2. Some material properties such as the Poisson's ratio and the shear modulus were established based on values derived from similar materials presented in Lee and Fernandez (2018) since they were not provided in the datasheets.

Table 1
HSC material properties.

Ply	E_1 [GPa]	E_2 [GPa]	ν	G_{12} [GPa]	t_{ply} [mm]	ρ [kg m^{-3}]
Satin Weave Glass fibre $E220$	18.3	18.3	0.02	3.9	0.09	1812
Satin Weave Glass fibre $E215$	29.3	16	0.2	3.9	0.152	1870
Satin Weave Glass fibre $E224$	31.4	7.12	0.2	3.9	0.265	1870

Table 2
HSC laminate layups.

Shell	Layup	Orientation	t_{shell} [mm]
1	$E220/E215/E220$	±45°/0°UD/±45°	0.332
2	$E220/\ E220/E215/E220/E220$	±45°/±45°/0°UD/±45°/±45°	0.512
3	$E220/\ E220/E224/E220/E220$	±45°/±45°/0°UD/±45°/±45°	0.625

The three shells, each suitable for the proposed SAR application, allowed the differences in the deployment velocity due to the different stiffnesses of the materials to be compared. The geometric properties of all the shells are the length $L = 1$ m, the width $b = 0.37$ m and the natural radius $R = 0.286$ m, as shown in Fig. 1(b).

In the first instance, to reproduce the actual deployment of the shell from a deployer, a double-flanged clamp was manufactured and used to rigidly constrain one edge of the shell. The clamp consists of a bottom and top part designed with a curved shape to accommodate the shell's natural curvature. Each flange was assembled with four laser-cut Plexiglas plates of 10 mm thickness that were rigidly centred together. This clamp was then screwed into a base support. The deployment plate was secured to the top flange. The other edge was left free to be flattened and coiled for the stowage process. Due to the presence of the ploy region, which is identified as the transition region between the flat and the curved part and is characterised by high-stress concentrations (Yang et al., 2018), the free edge was coiled until a certain distance from the clamped edge to avoid material damage. The initial configuration is shown in Fig. 2. In order to track the displacement during deployment, two retro-reflective markers were placed at the two corners of the shell's tip, which was then coiled up towards the shell's constrained edge with a drum. The retro-reflective part of the markers offset from the shell surface of 10 mm in the y-direction, as shown, with respect to reference frame, in Fig. 2. The shell was then secured with a string, acting as a burnwire hold-down release mechanism, before the drum was then removed. A third marker was placed on the clamped support to define the origin of the system of reference. Starting from a previous study conducted on the ploy region's impact on the shell's flexibility during the coiling process (Tresoldi et al., 2023a), 40 mm of the shell's root was constrained and the coiled shell was offset from the clamped edge by 160 mm. Hence, the total length accounted for during deployment was $L_d = 0.8$ m. The final radius of the coiling was 50 mm for the thinner shells, Shell 1 and Shell 2, and 60 mm for Shell 3. Once the shell was released, the markers' displacements were recorded and tracked by 12 infrared cameras that were positioned around the shell. The software used for object tracking was Vicon Nexus Tracker. Displacement and velocity data were collected with a sampling frequency of 375 Hz. The cameras were calibrated to a maximum error of ± 0.641 mm, which yields an error of $\pm\ 0.91 \times 10^{-3}$ m s^{-1} when considering error propagation in the calculation of the velocity within the software. By tracking the shell's tip path during deployment, it was observed that the shell's tip translated while uncoiling in the opposite direction to the fixed root in order for the shell to recover its extended undeformed state. In Fig. 3(a), it can be seen that the tip described an approximated spiral path from the starting point highlighted on the right where the shell is fully coiled to the endpoint on the left where the shell is fully deployed. The two markers travelled along paths that are similar and show a symmetry in the deployment shell path.

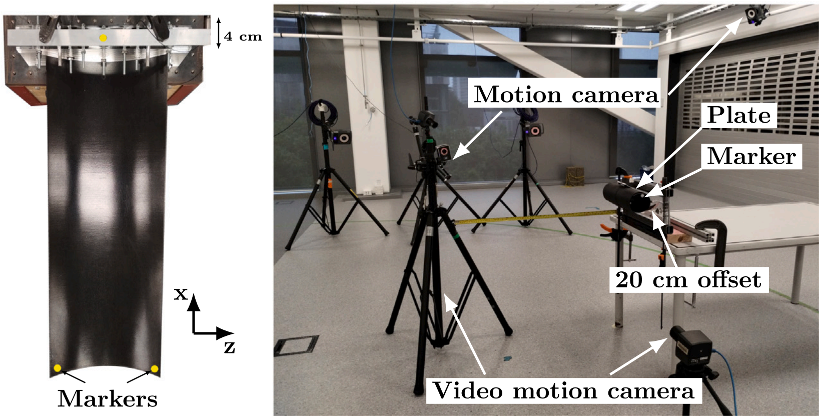

Fig. 2. Deployment testing set-up and markers' placement on the shell.

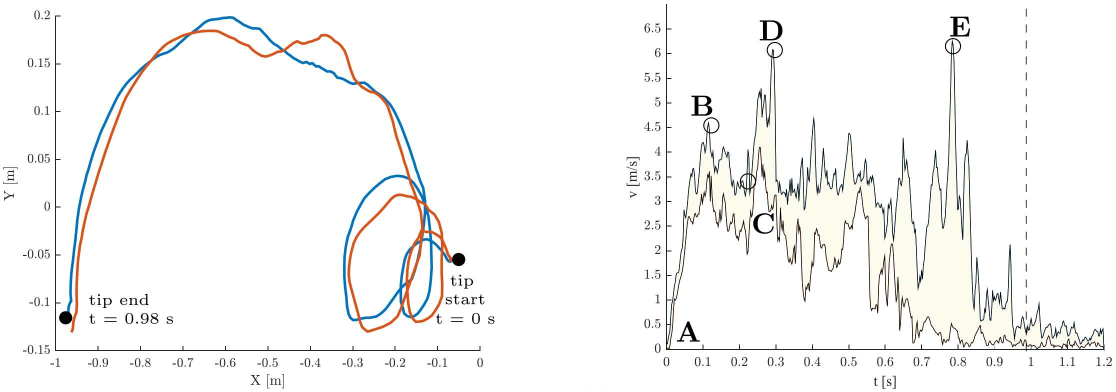

(a) Shell's tip path. Right marker is orange, left marker is blue.

(b) Shell's tip speed region between the minimum and maximum measurements. The region is given by the left marker solutions.

Fig. 3. Displacement and speed data collected from the retro-reflective markers during deployment of Shell 1.

Taking Shell 1 as an example, Fig. 3(b) shows the range of the speed's results collected from a series of tests conducted on Shell 1. The highlighted area was defined based on the minimum and maximum values of the peaks recorded by the left marker. As illustrated in Fig. 3(b), the very narrow band of solutions in the initial phase of the deployment showed that tests were accurately repeatable until B, while after D the area enclosed by the maximum and minimum speed values increased due to a more chaotic deployment process. The deployment occurred in approximately 0.98 s as highlighted in Fig. 3(b) with a vertical black dashed line and an initial oscillatory behaviour was identified until approximately $t = 0.3$ s. This region is identified by the letters A, B, C and D in Fig. 3(b). The elastic vibrations that occurred after $t = 1.2$ s are not shown Fig. 3(b) and not analysed in this study. A non-linear speed was related to the presence of the gravity force that acted against the shell's unrolling and translating. A plateau of the speed followed the first two peaks, highlighted as B and D, before another peak was captured at approximately $t = 0.78$ s, E. By analysing the corresponding times against a recorded video of the deployment, it was found that the initial speed peaks, B and D, occurred when the shell expanded and unrolled simultaneously. While the third peak, E, was identified at the time where the shell, after forming a natural "hinge", snaps to open up completely.

Unlike traditional bistable tape spring boom deployments, where the coiled part travels horizontally through an "unrolling carpet" process, in Fig. 4 it can be seen that the shell undergoes three main steps when deployed in a non-controlled condition: blossoming, uncoiling and stiffening. The blossoming and uncoiling occurred together due to the initial condition of $r < R$ and the shells' aspect ratio. In this case, it is approximately 12 times smaller than a generic tape spring of length 1 m and width 0.03 m. In the latter stage, the stiffness of the shell changes along the longitudinal axis as it recovers its transverse natural curvature from the tip and close to the root, where the shell is constrained, to the central part after forming the final hinge. Although only the deployment test carried out with one of the shells' configurations is reported here, it was found that the trend of the deployment path and speed presented in Figs. 3(a) and 3(b) was representative of all three of the shell designs.

3. Finite element model

3.1. Model setup

A FE Model was developed in ABAQUS/Standard 2022 to simulate the blossoming process of the shells and compare the blossoming speed with the testing. The shells' geometries were modelled with the material properties and layups given in Tables 1 and 2 by adopting classical lamination theory using the built-in standard ABAQUS tool. Dynamic implicit analysis was conducted and the velocity and displacement magnitude (V and U in ABAQUS) of the node located in the left marker's position during testing were requested as output of the simulation. The simulation consisted of six steps in which the boundary conditions were applied as follows:

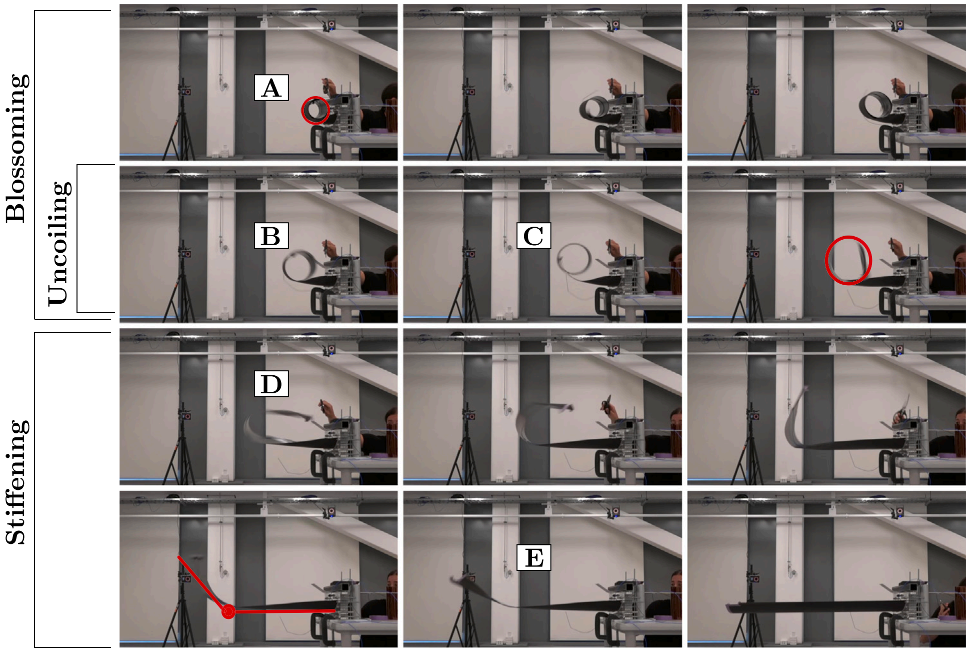

Fig. 4. Deployment frames of the DERCA's shell structure. Points A, B, C, D and E are highlighted in the different stages of the deployment.

- The shell's root is constrained in the six Degrees of Freedom (DoF) and the lateral edges of the free edge are flattened applying edge rotational displacements.
- Contact interactions are activated between the flattened edge and a deployment drum which is modelled as a rigid body.
- The deployment drum is released along the vertical direction while an initial rotational displacement is applied along the drum axis.
- The drum is constrained at the released position, and a rotational displacement along the drum axis is applied to allow the shell to coil on itself. The encastre at the root is released along the x-axis to allow the shell's translation.
- The fully coiled shell is constrained in the 6 DoF and a tangential friction of 0.2 is used to establish the contact with the deployment plate. The drum is then removed.
- Deployment is enabled by releasing all the shell's constraints apart from the shell's root, which is fully constrained at the two corners nodes only. Gravity is added in this step.

SR4 shell elements with an element size of $0.01\,\mathrm{m}$ (3610 elements) were used to mesh the shell. A general contact interaction was used with "Hard" contact property in the normal behaviour and a penalty of 0.1 for the tangential behaviour. A tension force was applied to the root edge using a shell edge load in the X-direction. Such tension was given opposite to the sliding of the shell towards the tip to reduce the spontaneous bending of the shell at its natural radius. During the deployment step, a damping factor of 0.02, which was tuned based on the experimental results, was added to the shell's material properties to reduce the oscillations of the structure and dissipate its energy during deployment. The deployment step is shown in Fig. 5 at different time steps during blossoming.

3.2. Model validation

To validate the FE model, the speed results and the blossoming time were compared to those of the tests. These comparisons are shown in Figs. 6, 7(a) and 7(b) where the test data of Shell 1 are taken as reference. In Fig. 6, it can be seen that the FEM well predicts the deployment time of the test with a slight delay that varies between $0.01\,\mathrm{s}$ and $0.02\,\mathrm{s}$ until the final stage of blossoming. The illustrated time frames were chosen by matching the tip's location between the FEM and experiment results. In Fig. 7(a), the deployment path taken from the left marker's data is compared to the FEM path result. It can be seen that the marker's trajectory is very well reproduced by the FEM displacement. To note is that the distance of the retro-reflective sensor from the shell surface where the marker was attached, as explained in Section 2, was taken into account in the FEM analysis by reproducing the offset with a multi-point constraint located at the shell's tip edge. This agreement of the results is also shown in Fig. 7(b), where the tip deployment speed results are compared until blossoming. The FEM tip result reproduced the oscillatory trend from testing, showing a very good agreement in the final part of the blossoming where the speed and deployment time are consistent with the test data from approximately $t = 0.09\,\mathrm{s}$ until the tip blossoming time at $t = 0.254\,\mathrm{s}$. In the initial part of the curve, the FEM curve follows the test speed trend, although higher deployment energy is noticeable in the FEM prediction. Such a difference can be related to the dissipative factors (i.e., damping factor, shell's layers and deployment panel friction coefficient) used in the simulation and the difficulty in predicting the exact shell's behaviour due to the accuracy of the shell's ABD matrix, given that some of the material properties were estimated to implement the FE model. Finally, it can be seen that the tip blossoming time is predicted very well by the FEM with only $\pm\,0.78\%$ difference with the test data.

4. Expanding circle model

4.1. Analytical model

Starting from test observations, the initial stage of the deployment is assumed to be a standalone event in which the shell blossoms and uncoils freely. To describe the occurrence of blossoming and predict the blossoming speed, the shell is considered to be rolled up along the length and then released. In this model, the transition region that extends from the flat to the curved part is neglected, and initially, the fixed boundary condition is assumed to be the centre of the coiled structure. Such a point is the origin O of the reference system for this model. Given a circle of length l and initial radius smaller than the natural radius $r_1 < R$, blossoming is modelled as an expanding motion in which a generic point P, defined on a circle at a certain angle θ at $t = 0$, moves radially and tangentially to a bigger circle of radius $r_2 >$

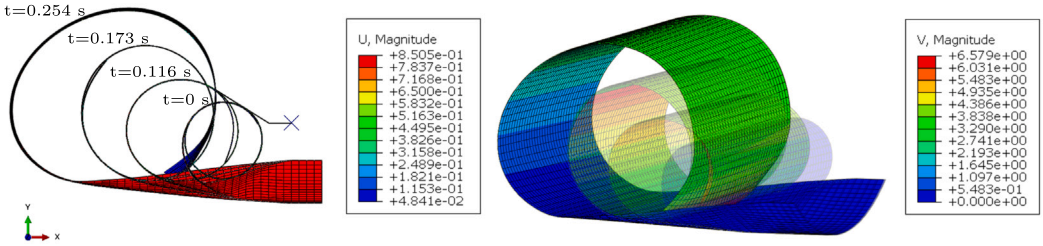

Fig. 5. FEM deployment step during blossoming.

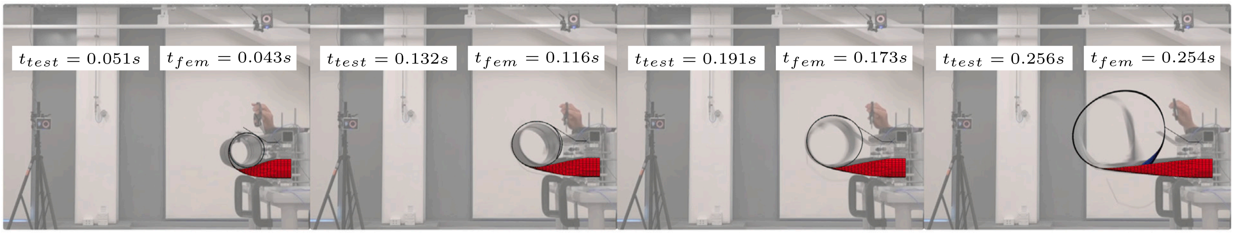

Fig. 6. Deployment time comparison of the FE model and testing.

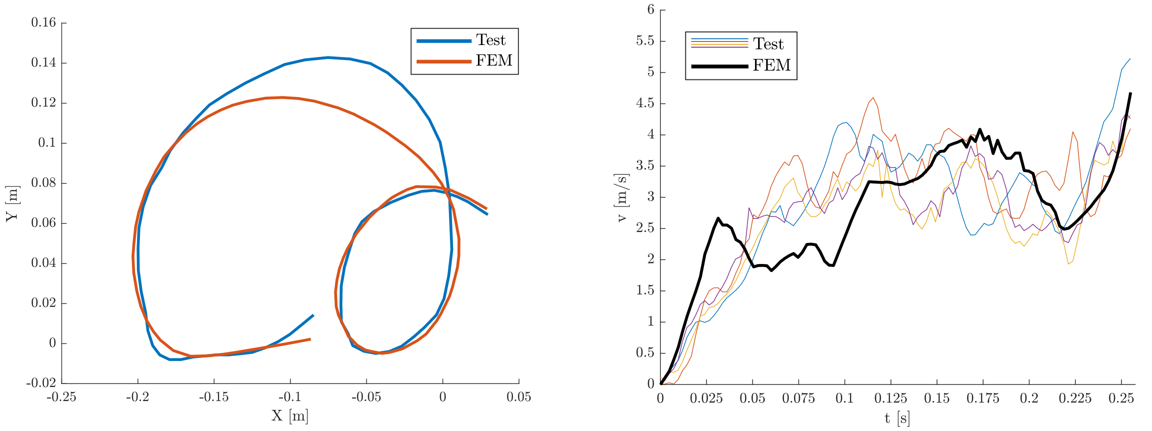

(a) Deployment path of the FE model during blossoming compared to testing.

(b) Shell's tip speed from testing compared to the FEM solution.

Fig. 7. FEM displacement and speed compared to testing of Shell 1.

r_1 at $t > 0$, as illustrated in Fig. 8. To maintain the physical length of the shell, it is assumed that as the radius increases the angle subtended by the shell decreases. Given the same length and different radii, it is also assumed that for every $r < r_2$, the increment of the radius given by the overlapping is neglected. This can also be assumed given that the shell's thickness is three orders of magnitude smaller than the shell's length and the strain energy change is minimal. Having all the points on the same radius with respect to the origin of the reference system at each time $t > 0$, the generic point P is considered and defined in the polar plane by its position and velocity vector as:

$$\mathbf{r}_P = r\hat{\mathbf{r}} \tag{1}$$

$$\mathbf{v}_P = \frac{d\mathbf{r}_P}{dt} = \frac{dr}{dt}\hat{\mathbf{r}} + r\frac{d\hat{\mathbf{r}}}{dt} = \dot{r}\hat{\mathbf{r}} + r\dot{\theta}\hat{\theta} \tag{2}$$

where $\hat{\mathbf{r}}$ is the unit vector that defines the positive direction along the radius and $\hat{\theta}$, orthogonal to it, defines the positive direction of rotation by the angle θ. As in Seffen and Pellegrino (1999), a Lagrangian approach is used to express the equations of motion of the coiled HSC shell with equation Eq. (3).

$$\frac{d}{dt}\left(\frac{\partial \mathcal{L}}{\partial \dot{q}_i}\right) - \left(\frac{\partial \mathcal{L}}{\partial q_i}\right) = Q_i. \tag{3}$$

In this case study, the generalised coordinates of the system q_i are r and θ, and the non-conservative generalised forces Q_i acting on the system are the air drag force and the friction generated between the shell's layers. Given that the length is maintained as the radius changes and the point P runs along a circular motion, a relationship between r and θ can be stated so that $\theta = l/r$. Such an assumption allows the generalised coordinates of the system to be reduced to one, in this case, r. In order to define the Lagrangian of the system as $\mathcal{L} = T - V$, the total kinetic and potential energy, T and V, respectively, are defined as:

$$T = \frac{1}{2}\int_0^l \rho_m v^2\, dl = \frac{1}{2}\rho_m \int_0^l \left(\dot{r}(t)^2 + r(t)^2\dot{\theta}^2\right) dl \tag{4}$$

$$V = \frac{1}{2}b\int_0^l \left(\frac{D_{11}}{r(t)^2} - \frac{2D_{12}}{r(t)R} + \frac{D_{22}}{R^2}\right) dl + \rho_m g l \int_0^{2\pi n_{rev}} r(t)\,(1+\sin(\theta))\, d\theta \tag{5}$$

where ρ_m is the mass density per unit length, and l is the shell's coiled length. Since l is constant, $\theta(t) = l/r(t)$ and $\dot{\theta} = -l/r(t)^2 r(\dot{t})$ can be substituted in the T and V. The potential energy V is expressed by the elastic energy stored in a curved section (Calladine, 1983) that is bent at a given radius r and the gravitational potential energy that

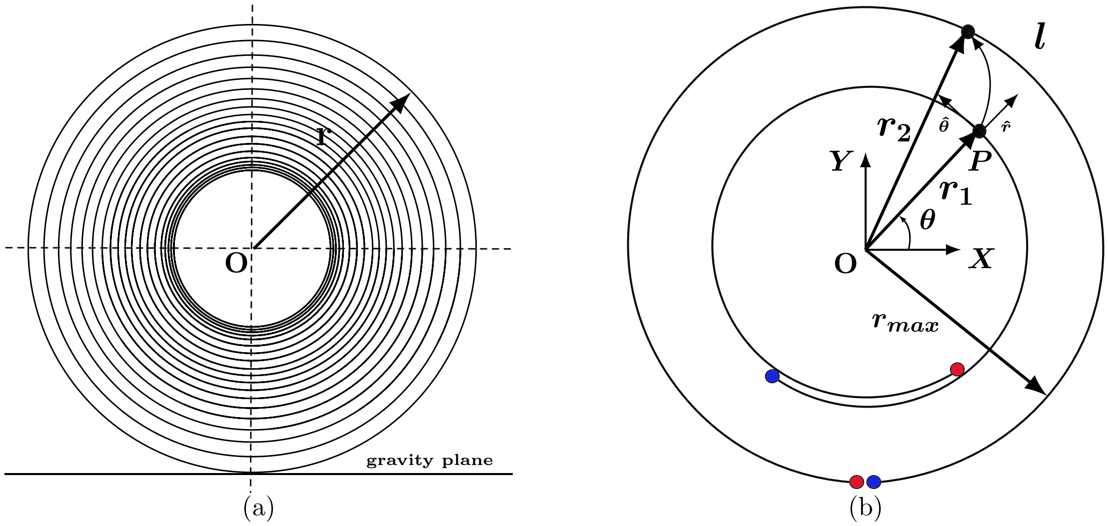

Fig. 8. Expanding circle model.

acts on the system at each coiled radius with respect to the gravity plane in Fig. 8(a). Where $n_{rev} = r_{max}/r(t)$ is the number of overlapping revolutions and $r_{max} = l/(2\pi)$. Therefore, when $r = r_{max}$, the shell has a circular shape with no overlapping layers, as shown in Fig. 8(b). The other parameters that are in Eq. (5) are the flexural stiffness terms of the material ABD-matrix D_{11}, D_{12}, D_{22}. Hence, after submitting Eqs. (4) and (5) with the length constraint to the Lagrangian of the problem $\mathcal{L}$, the equation of motion for $Q_i = 0$ is:

$$\begin{aligned}&-\frac{\rho_m l^3 \dot{r}(t)^2}{r(t)^3} + \frac{1}{2} bl \left(-\frac{2D_{11}}{r(t)^3} + \frac{2D_{12}}{Rr(t)^2}\right)\\ &+ \rho_m g l \left(1 - \cos\left(\frac{l}{r}\right) - \frac{l}{r}\sin\left(\frac{l}{r}\right)\right) +\\ &\left(\rho_m l \left(1 + \frac{l^2}{r(t)^2}\right) \ddot{r}(t)\right) = 0\end{aligned} \tag{6}$$

It is assumed that the normal flow on the shell surface generates drag to introduce the effect of air drag in the model. The generalised Rayleigh's dissipation function D can be used to define the dissipation force acting on the system. D is defined as:

$$D = \frac{1}{n+1}\sum_j c_j v_j^{n+1} = \frac{1}{6}\rho_{air} C_D A \dot{r}^3 \tag{7}$$

where j is the number of objects of the system, in this case $j = 1$, $n = 2$ describes the force-velocity dependence, $c = 1/2\rho_{air}C_D A$ is the dissipation coefficient and $v = \dot{r}$ is the velocity of each object. In this configuration, the shell's tangential velocity does not affect drag, as the wet area A is considered normal to the airflow. Such an area changes proportionally to r as $A = 2\pi r(t)b$. The other terms of the dissipation coefficient are ρ_{air}, which is the density of air and C_D, which is the drag coefficient defined by the cross-section. As reported in the literature for tape spring cases (Seffen and Pellegrino, 1999), C_D for semicircular shells is considered to vary between 2.3 and 1.1 (Aziz et al., 2008).

Another dissipation effect that is included in the model is the friction generated between layers during blossoming. To define it, the friction is assumed to act normal to the surfaces between the outer r_{out} and the inner layer r_{in} and is expressed by the centrifugal force as:

$$F_N = -\rho_m l \dot{\theta}^2 \left(r_{in} - r_{out}\right) = \rho_m l \dot{\theta}^2 \left(\frac{r_{max}}{r}\right) h \tag{8}$$

where r_{max}/r is the number of overlapping turns, and h is the shell thickness. Substituting in Eq. (8) for r_{max} and $\dot{\theta}$, a new dissipation function F_R, Eq. (9), can be derived for the friction energy:

$$F_R = \frac{1}{3}\mu F_N \dot{r}(t) = \frac{hl^4 \mu \rho_m \dot{r}(t)^3}{6\pi r(t)^5} \tag{9}$$

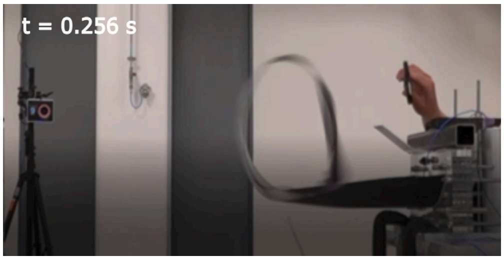

Fig. 9. Blossoming final condition for Shell 1 at $r = r_{max}$.

where μ is the friction coefficient that is assumed to be 0.2, which is the friction coefficient value used in similar composite materials (Subramaniam et al., 1991; Zhang et al., 2014; Alotaibi et al., 2021). Therefore, the equation of motion when the generalised force $Q_i \neq 0$ is:

$$\begin{aligned}&-\frac{\rho_m l^3 \dot{r}(t)^2}{r(t)^3} + \frac{1}{2} bl \left(-\frac{2D_{11}}{r(t)^3} + \frac{2D_{12}}{Rr(t)^2}\right)\\ &+ \rho_m g l \left(1 - \cos\left(\frac{l}{r}\right) - \frac{l}{r}\sin\left(\frac{l}{r}\right)\right) +\\ &\left(\rho_m l \left(1 + \frac{l^2}{r(t)^2}\right) \ddot{r}(t)\right) = -b\pi r(t)\rho_{air} C_D \dot{r}(t)^2 - \frac{hl^4 \mu \rho_m \dot{r}(t)^2}{2\pi r(t)^5}\end{aligned} \tag{10}$$

The integration of the nonlinear differential equation Eq. (10) is performed numerically to resolve the equation of motion using Matlab. In both motion states, frictionless and with dissipation, this model is valid until $r = r_{max}$, the condition at which blossoming, described as an expanding circle process, ends. For simplicity, this condition is called t_{blos} and will identify the end of the blossoming process for the rest of the paper. For example, from Shell 1 testing, t_{blos} was observed at $t = 0.256$ s, the time at which the shell gets to the end of the uncoiling process, and the shell's tip reaches the position that describes a circle with no overlapping layers, as captured in Fig. 9.

4.2. Dragging effect: Convective reference frame

As described in Section 4.1, the governing equation in Eq. (10) is solved in the (x, y) fixed reference frame, as also shown in Fig. 8(a). To consider the actual boundary condition of the shell's stowage configuration during testing imposed by the deployment plate and the clamping mechanism, a transformation of coordinates is applied by

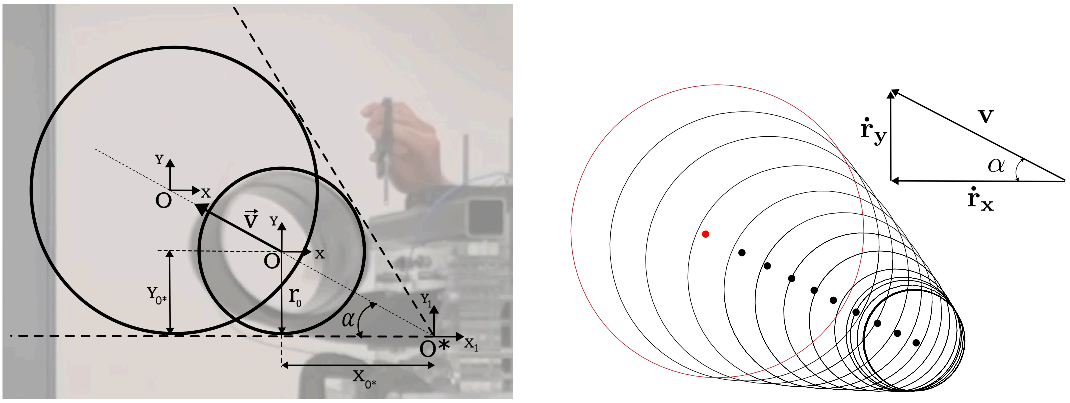

(a) Spatial reference frame (x, y) and material reference frame (x_1, y_1) with a new constrained point in O*.

(b) Schematic sequence of translated circles given the convective reference frame and the triangle of velocities.

Fig. 10. Convective reference system.

introducing a different constrained point as the origin of a new frame of reference (x_1, y_1). Such a frame of reference is chosen and translated from the circle's centre O to the bottom-right corner O^*, where the shell's root is rigidly fixed during the test. To express the deployment path and speed relative to O^* in the new frame (x_1, y_1), the solution provided by Eq. (10) is used by adding a transport motion (Kirchägner, 2016; Filippi and Carrera, 2017). Following the terminology in Hetzler (2009), the (x, y) reference frame is referred to as the spatial (or convective) frame, while (x_1, y_1) is the material frame. As schematically illustrated in Fig. 10, the spatial frame is not fixed; rather, it moves with respect to the material frame at a certain angle from the x-axis, as observed from the test data in Fig. 4.

Based on the experimental setup, some geometrical assumptions are made to define (x, y) relative to (x_1, y_1), as shown in Fig. 10. The initial distance of the origin O* from O is given by the coordinates x_{0*} and y_{0*} that are calculated as $(r_0/tan(\alpha), r_0)$. Where $\alpha = 26°$ is an initial angle, as measured from the test setup, between the line intersecting O and O* and the x-axis. The triangle of velocities is shown in Fig. 10(b), where it can be seen the relationship between the horizontal and vertical components of the velocity as a function of the angle α such that $\dot{r}_x = \dot{r}_y/tan(\alpha)$ and $\dot{r}_y = \dot{r}$. Hence, the transformation of coordinates is applied such that:

$$x_1 = x - x_{0^*} - \int_0^t \dot{r}_x dt = x - x_{0^*} - \frac{1}{\tan(\alpha)} \int_0^t \dot{r}(t) dt = x - x_{0^*} - \frac{1}{\tan(\alpha)}(r(t) - r_0) \tag{11}$$

$$y_1 = y + y_{0^*} + \int_0^t \dot{r}(t) dt = y + y_{0^*} + (r(t) - r_0) \tag{12}$$

where x_1 and y_1 are the coordinates of a generic point in the new frame of reference. The velocity terms are convective terms and express the relative velocity between the two frames. Eqs. (11) and (12) are a combination of the velocity terms, the position solutions in the inertial (fixed) frame of reference, x and y, and the initial positions x_{0^*} and y_{0^*}.

4.3. Results and discussion

This section compares the results obtained from the analytical model to the experiments conducted on the three shell layups. As described in Sections 2 and 4.2, due to the boundary condition, the tip travelled along an approximated spiral path in which the centre of the local circle formed by the coiled shell translated as the shell blossomed. Such a translation occurred as the deployment was enabled, hence involving the blossoming phase. The displacement of the shell's tip tracked during the test in the in-plane X_1 and Y_1 directions is shown in Fig. 11. Concerning Shell 1, as shown in Fig. 9, at t_{blos} $t = 0.256$ s, the shell reached the condition where there were no overlapping layers, and the blossoming process finished. The shell's tip position at the corresponding time is highlighted in blue in Fig. 11. The analytical tip's displacement solutions that were derived with Eq. (10) until t_{blos}, are shown in Figs. 12(a) and 12(b), for the fixed central and convective reference frame, respectively. In Fig. 12(a), it is clear that by maintaining the origin of the reference frame fixed in the centre of the circles, the path identified by the shell's tip describes a spiral that runs outwards for $r(t)$ increasing. Whereas, by implementing a convective reference frame as in Fig. 12(b), all the positions that the shell's tip assumes during blossoming belong to circles that translate for $r(t)$ increasing with respect to a new constrained point defined as in Fig. 10(a). The tip displacement predicted by the analytical model of the Shell 1, 2 and 3 until t_{blos} is illustrated in Fig. 13 along with the experimental results.

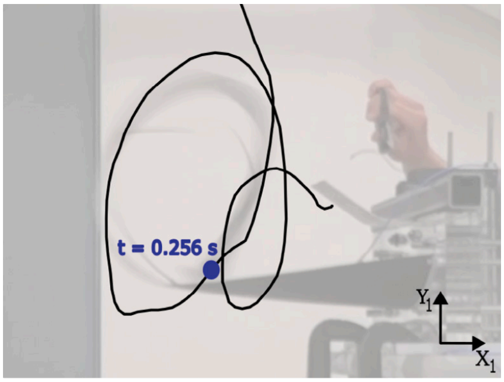

Fig. 11. Shell's tip path during blossoming tracked by retro-reflective markers. The frozen image behind is Shell 1 at t_{blos}.

It can be seen that the results from the analytical solution predict the deployment trend well and show a good correlation with testing of the number of turns and deployment path. The latter correlates with the tests' deployment path better than the fixed frame path prediction. In fact, the change of coordinates applied with the convective frame produced a translation of the shell's points that led to the shaping of a shifted spiral as in the test data. At the same time, it can be seen that the deployment's displacement described by the analytical model travels on a more circular path shape than the tests' results. These, in contrast, show less uniform paths which are "stretched" in the horizontal direction. From test observations, this was due to the presence of the

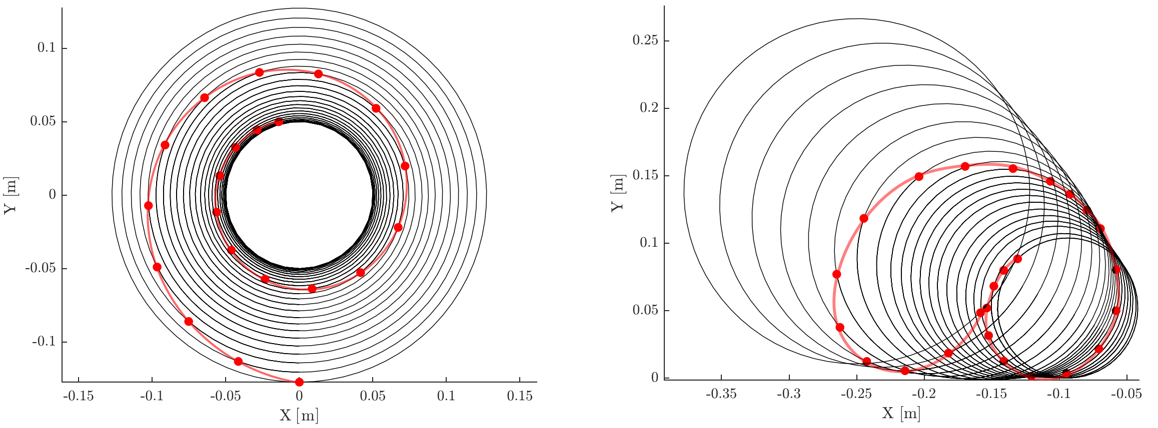

(a) Tip path with the fixed central reference system creating a spiral.

(b) Tip path with the convective reference system creating a shifted spiral.

Fig. 12. Expanding circle model tip path solution described at growing radii.

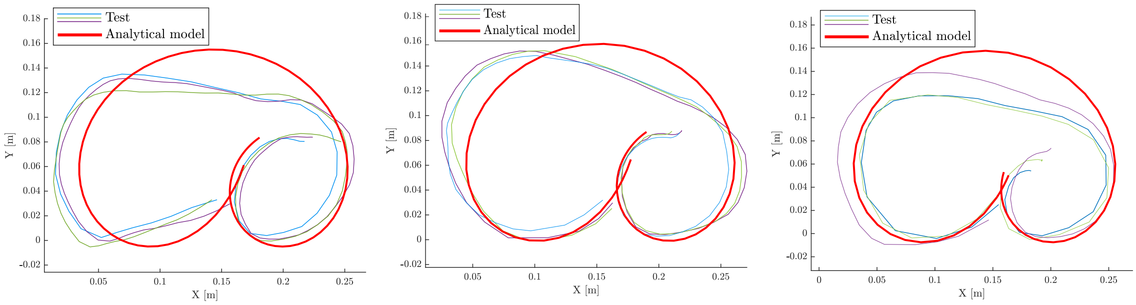

(a) Shell 1

(b) Shell 2

(c) Shell 3

Fig. 13. Analytical tip path of the analytical model compared to deployment testing.

ploy region, which was neglected in the model, that forced the shell to blossom and translate faster to recover its extended state. Concerning the deployment starting and blossoming ending position, the analytical predictions are coherent with the test data. However, it can be seen that the starting position resulting from the analytical model only approximates the initial positions of the test curves. In fact, due to the difficulty in repeating the same test set-up with high accuracy, the initial markers' position slightly varied between the tests, challenging the estimation of the exact starting position to be implemented in the analytical model. From the resolution of Eq. (10), the analytical model also provided an estimation of the system's speed based on the radial and tangential components of the velocity calculated at each radius. Of course, using a fixed system of reference, all the points that belonged to growing circles had the same speed at the same radius. However, given the real boundary conditions of the stowage configuration, the local speed of the system was expected to vary along the shell's length. In the analytical model, this condition was achieved using the convective reference frame, as described in Section 4.2 and by differentiating Eqs. (11) and (12). This enabled the speed to vary based on the different positions that all the points had as a function of time with respect to the new constrained point O^*. Taking Shell 1 as an example, the tip's speed and path estimated by the model with Eq. (10) is shown in Figs. 14(a) and 14(b) and is compared to the case where gravity and the non-conservative generalised forces are not accounted for in the system. By resolving Eq. (6), the results from the analytical model showed that the condition of $r = r_{max}$ occurred at $t = 0.261$ s. Introducing dissipative effects and gravity, it can be seen that there is a small change in the speed and deployment time.

It is to be said that while the addition of the dissipation effects did not significantly impact the tip's speed result, the presence of gravity produced an oscillatory speed behaviour and an increase in the deployment speed. The effect was a slower speed at the beginning of the deployment and faster at the end. Therefore, with the above-mentioned parameters, air drag and the friction between the shell's layers did not cause a significant loss of the system's internal energy; rather, gravity had the most energetic effect. In the absence of some material properties and friction data, the speed result was estimated for a range of values of D_{11}, D_{12}, C_D and μ. Based on the values found in the literature, C_D was varied from 1.1 to 2.3 as in Seffen and Pellegrino (1999), while μ was varied of ± 20% of the value that was used for similar composites in Subramaniam et al. (1991), Zhang et al. (2014) and Alotaibi et al. (2021). The bending stiffness terms D_{11} and D_{12}, were also varied in the range of ± 5% of the value calculated from datasheet. Such a range was estimated by changing G_{12} and ν of ± 20%, as they were not provided in the material properties. The area of the potential speed solutions is illustrated in Figs. 15(a), 16(a) and 17(a) and compared to a series of three tests conducted on Shell 1, 2 and 3, respectively. For all the shells, the upper and lower limits were defined based on the maximum and minimum values of these parameters. It can be seen that the lower bound, coloured in blue, corresponds to the smallest deployment speed solution that was obtained for the smallest bending stiffness value and the highest values of air drag and friction coefficient. Whereas the upper bound, shown in green, represents the shortest deployment time solution. This condition was reached when the shell was assumed to be at the highest potential state of stiffness, and the dissipation effects had the lowest impact on the system. For each shell, the red curve was found to result in the speed solution that had the smallest deviation from test curves for the selected parameters of $C_D = 1.1$, $\mu = 0.2$ and the calculated value of D_{11} and D_{12} from the datasheet. Hence, such a speed result

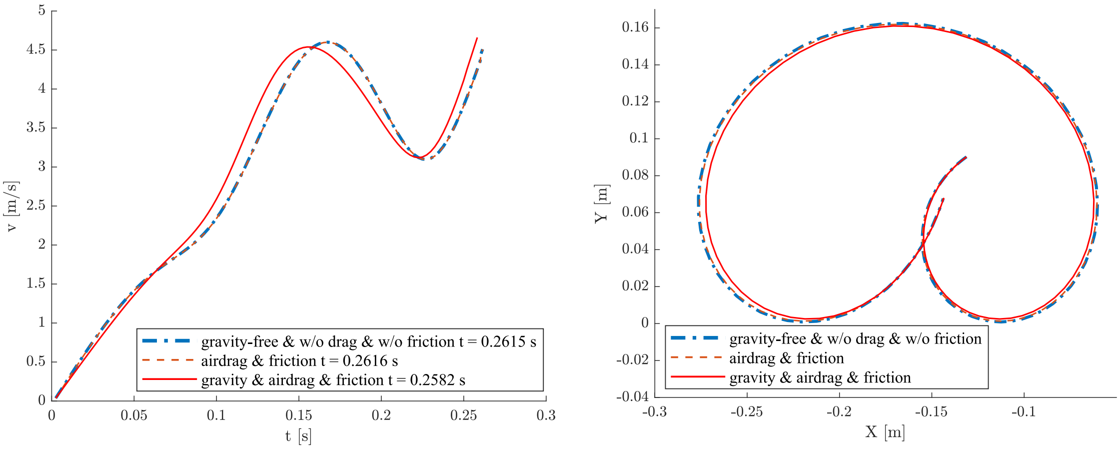

(a) Tip's speed. (b) Tip's path.

Fig. 14. Tip speed and path comparison for Shell 1 predicted by the analytical model for gravity-free cases and absence of dissipative forces and gravity, $C_D = 1.1$ and $\mu = 0.1$.

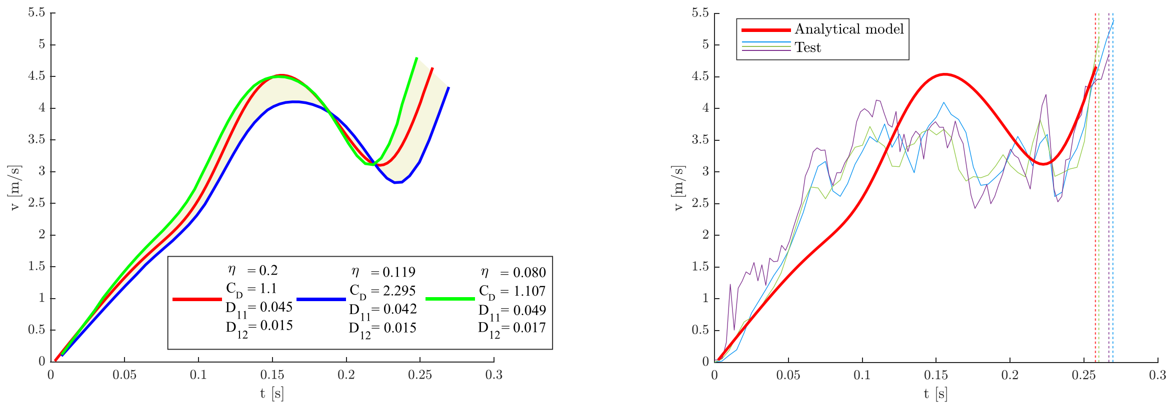

(a) Area of the analytical tip speed solutions for Shell 1 generated by varying μ, C_D, D_{11} and D_{12}.

(b) Tip speed comparison with t_{blos} highlighted by red and coloured dashed lines, respectively.

Fig. 15. Shell 1 speed results.

was compared with the experimental data and is reported in Table 3 along with the maximum and minimum estimated values obtained by varying the selected parameters. The comparison with testing is shown in Figs. 15(b), 16(b) and 17(b) for Shell 1, 2 and 3, respectively. The results extracted from the markers, used during testing to evaluate the velocity magnitude at the tip, provided speed data every 0.02 s over the deployment time. All the shells' velocities collected from the tests are shown until t_{blos}. Generally, the series of test curves conducted on the three shells shows that the tip speed increased with an undulating trend until t_{blos}, where the curve reached the highest speed value. The fluctuation has a cubic function trend with two turning points where the speed changes direction.

Taking the Shell 1 test as an example, Fig. 18 illustrates the positions of these points and the corresponding shell's behaviour captured from the FE simulation of the deployment process. Based on the FE model and test data, it was observed that the turning points occurred due to the shell's centre horizontal translation while blossoming and uncoiling. The potential gravitational energy of the system and the physical stowage's constraints were also assumed to contribute to generating this trend. It was found that the shell expanded from $r_A = 0.05\,\mathrm{m}$ to $r_B = 0.125\,\mathrm{m}$ by increasing its speed until point B. At this turning point, the shell's centre started translating to the left while blossoming, causing a deceleration until point C. This event is captured by Fig. 18 which shows that the uncoiled shell's part extended from $l_B = 0.306\,\mathrm{m}$ to $l_C = 0.36\,\mathrm{m}$ due to the horizontal translation and blossomed until $r_c = 0.165\,\mathrm{m}$. After point C, the shell ended the blossoming process by expanding until $r_{max} = 0.205\,\mathrm{m}$ and accelerating again until t_{blos}. By comparing the test results shown in Figs. 15(b), 16(b) and 17(b), it can be seen that the first turning point occurs at different times for the three shells by slightly changing the curve's concavity up or down at different velocities. For Shell 1, as a percentage of the overall blossoming time, the concavity change developed closer to t_{blos} and in a shorter time than for Shells 2 and 3. In these cases, the first turning point occurred faster than in Shell 1, leading to a larger plateau. This difference is related to the different shells' material properties and shows that the stiffer the shell is, the more it translates.

Coherently with testing, it can be seen that the analytical solutions follow the increasing and undulating speed trend of testing until t_{blos}, capturing well the change of concavity of the test curves at the corresponding turning points. The initial part of the curve predicts the shell's speed and deployment time very well for all the shells by correlating with test results until the first turning point is reached. This is because, as per Fig. 14, the initial deployment is mainly driven by blossoming. After this point, the usage of the convective reference frame in the derivation of the shell's speed allowed to implement the shell's translation developing after point B resulting in an oscillatory behaviour of the analytical curves until t_{blos}. For Shell 1 the first turning point is reached at $t = 0.15\,\mathrm{s}$, differing from the test predictions by approximately $0.04\,\mathrm{s}$. A very good correlation with testing can be found at the second turning point that occurs at $t = 0.23\,\mathrm{s}$, as shown in Fig. 15(b). Due to the different material properties between the shells that the model accounts for, for Shell 2 and 3, the analytical model

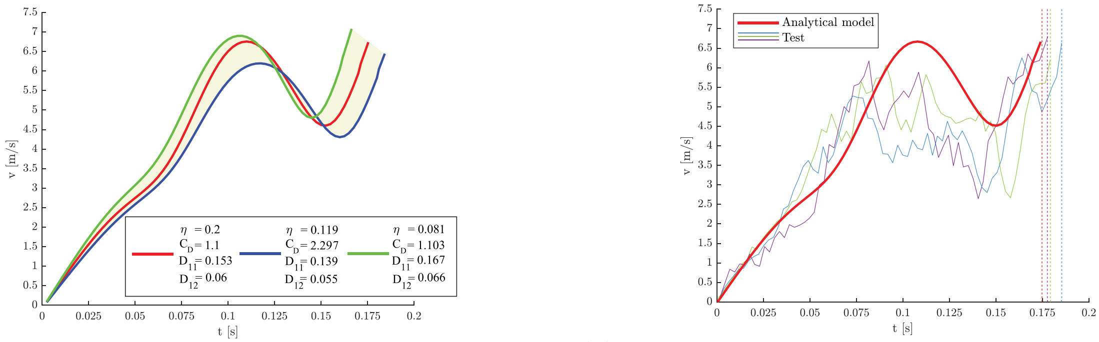

(a) Area of the analytical tip speed solutions for Shell 2 generated by varying μ, C_D, D_{11} and D_{12}.

(b) Tip speed comparison with t_{blos} highlighted by red and coloured dashed lines, respectively.

Fig. 16. Shell 2 speed results.

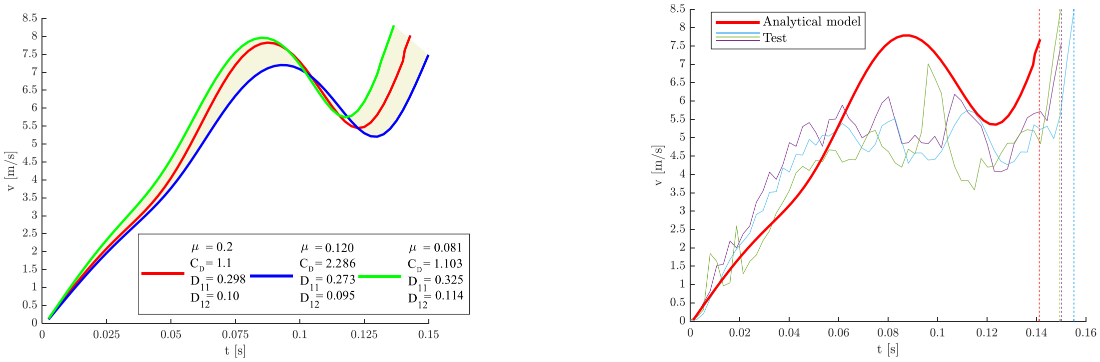

(a) Area of the analytical tip speed solutions for Shell 3 generated by varying μ, C_D, D_{11} and D_{12}.

(b) Tip speed comparison with t_{blos} highlighted by red and coloured dashed lines, respectively.

Fig. 17. Shell 3 speed results.

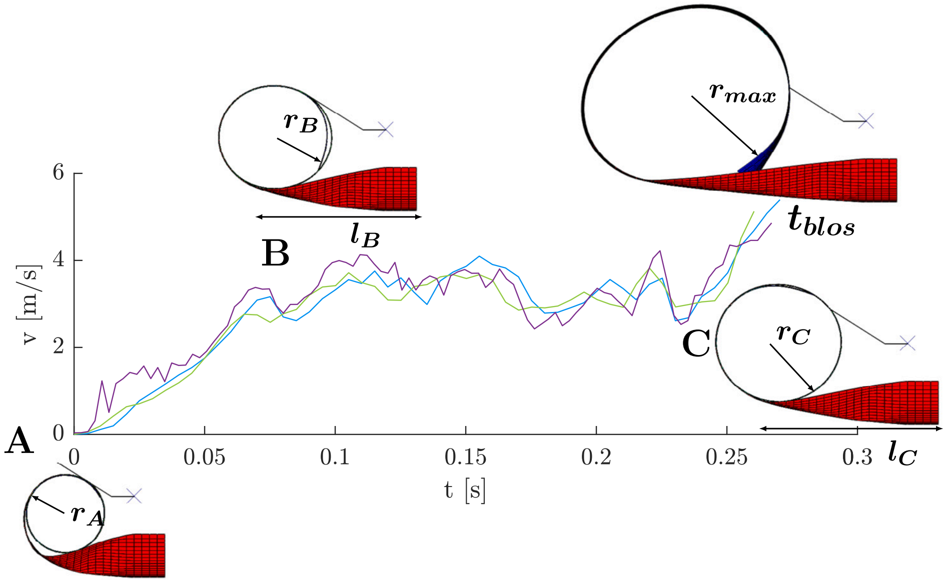

Fig. 18. Shell 1 speed tests results until t_{blos} with FE model deployment frames captured at the curve's points A, B, C and t_{blos}.

predicts the turning points to occur earlier than Shell 1 at $t = 0.11$ s and $t = 0.09$ s, for the first turning point and at $t = 0.16$ s and $t = 0.13$ s, respectively, for the second turning point, deviating from test data by 0.03 s only. Such a sensitive change, due to different physical properties, is well predicted in the analytical model. Indeed, as the shell thickness increased from Shell 1 to Shell 3, a higher deployment speed and a shorter deployment time were expected. From the speed comparison with the analytical curves at t_{blos}, the speed increased from 4.661 m s^{-1} for Shell 1 to 6.738 m s^{-1} for Shell 2 and 8.028 m s^{-1} for Shell 3 at the corresponding descending blossoming times of

0.258 s, 0.175 s and 0.142 s, respectively. The test results are collected in Table 3, showing good agreement with the analytical predictions of the maximum velocities occurring at t_{blos}, with less than 10% difference for all the shells. It can also be seen that the deployment time results differ less than 0.8% with Test 1 and 2 for Shell 1, 1% and 5% for Shell 2 and 3 with Test 1, respectively. Overall, the results predicted by the analytical model correlates well with the experimental results. However, differently from what occurred during testing, the plateau of the speed produced by the shell's translation is less predicted by the analytical model, showing a more evident deviation of the curve's trend from testing for the stiffer shells, Shell 2 and 3. This difference was related to the different shells' material properties and the accuracy of the shell's ABD matrix implemented in the analytical model, given that some of the material properties were estimated. Such a difference was also related to an underestimation of the total potential strain energy accounted for in the model, given that the stretching strain energy and the energy stored in the ploy region (Tresoldi et al.) are neglected in this study. Furthermore, as observed from different time frames, the assumption that the shell expands as a circle breaks down as the solution gets close to t_{blos}.

5. Multi-pendulum system model

5.1. Analytical model

5.1.1. Initial conditions

The analytical model presented in this section aims to describe the second phase of the deployment and compare the results of the deployment speed with testing. This phase has been defined as the "stiffening" phase in Section 2. In fact, after t_{blos}, the assumptions that lay the foundations of the expanding circle model are no longer valid. As captured in Fig. 4, as the blossoming process ends, the shell stops resembling a circle, and the deployment continues in a more chaotic way until the shell recovers its transverse natural curvature and structural stiffness. The "stiffening" phase of the deployment is also less repeatable and more sensitive to the initial setup which is shown in Fig. 3(b) by the results diverging. This divergence can be seen by the increased range of speed values for a given time, or, in another way, by the increased area. Starting from test observations, in this phase, the shell's structure passes from a closed "C" shape to an open "L" shape before extending completely, as captured from the Shell 2's deployment in Fig. 19.

When passing from one shape to the other, the shell locally changes its stiffness from a lower value where it is still flat to a higher value where it returns crosswise curved. Such a stiffness-changing behaviour can also be seen in tape springs that, under equal-and opposite-sense bending moments, form a characteristic hinge before straightening, as in Seffen and Pellegrino (1999). To describe the tape springs' deployment that has been bent, the authors split the tape into two straight parts by a single localised elastic fold whose motion along the tape length is resolved with a Lagrangian approach in a two-dimensional system. In their study, the fold is assumed to propagate along the longitudinal direction until it disappears. Similarly, in this model, the shell is split into n bars connected by $n+1$ point hinges that locally act as independent two-dimensional spring-damper systems. This type of system is based on a Hencky bar-chain/net model (Wang et al., 2020c) in which the shell's structure is discretised into a finite number of rigid elements that are joined together by elastic rotational springs and dampers, and that rigidly behave like a multi-pendulum system. Unlike in Seffen and Pellegrino (1999), in this case, the folds that occur along the chain of rigid elements disappear by unfolding based on the local stiffness variation of the bars. In fact, depending on the angles that each bar assumes during deployment, the shell's stiffness varies proportionally to its moment–rotation relationship. The final shell's state of energy at t_{blos} is considered the starting point to define the initial configuration of this model. From the expanding circle model, at this instant, the shell is a perfect circle and has reached such a shape by increasing its total kinetic energy T and decreasing its total potential energy V. The energy state at t_{blos} for Shell 1, 2 and 3 is shown in Fig. 20.

To implement the initial conditions of the joints and bars' positions, the end state of V, V_{min}, is used to evaluate the initial value of the multi-pendulum stiffness. In fact, the initial stiffness k_i of all the torsional springs connecting the n-bars is estimated by Eq. (13):

$$k_i = \frac{2V_{min}}{n\left(\Delta\theta_i^2\right)} \tag{13}$$

where $\Delta\theta_i$ is the initial position angle for all the bars, and it is given by Eq. (14):

$$\Delta\theta_i = 2\pi/n. \tag{14}$$

Concerning the initial velocities $\dot{\theta}_{n_i}$ of each n-bar, they can be estimated with Eq. (15) by considering the displacement angle $\Delta\gamma_n$ of each n-bar between the last two steps of the integration of the expanding circle model, that is at the time $\Delta t = t_{blos} - t_{blos-1}$. where t_{blos-1} is the time step at the iteration previous to t_{blos}.

As shown in Fig. 21 for a $n = 10$ bar system, $\Delta\gamma_n$ can be calculated geometrically. Given the positions X and Y of a bar at t_{blos} and t_{blos-1}, $\Delta\gamma$ is calculated with the slopes of the two lines passing through the bar's positions at t_{blos} and at t_{blos-1} and by using the trigonometric tangent function. Given the slopes $g_{t_{blos-1}}$ and $g_{t_{blos}}$, the angle $\Delta\gamma_n$

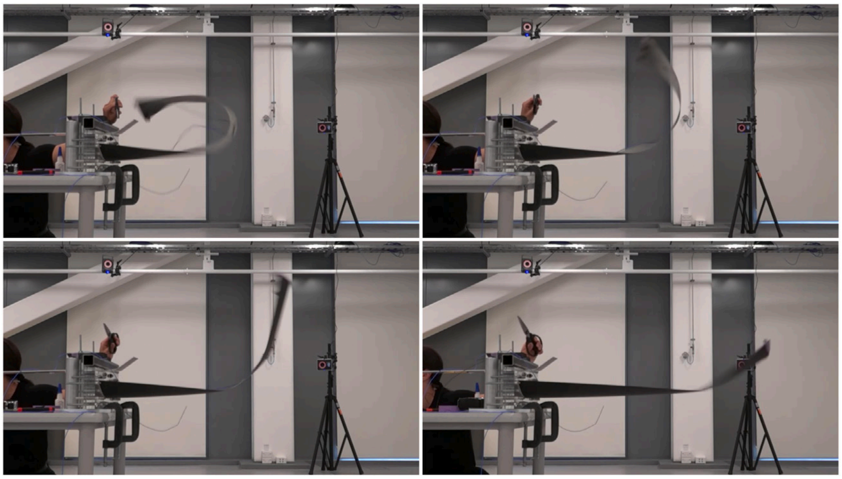

Fig. 19. Second phase of the deployment where Shell 2 passes from a "C" to an "L" shape before extending.

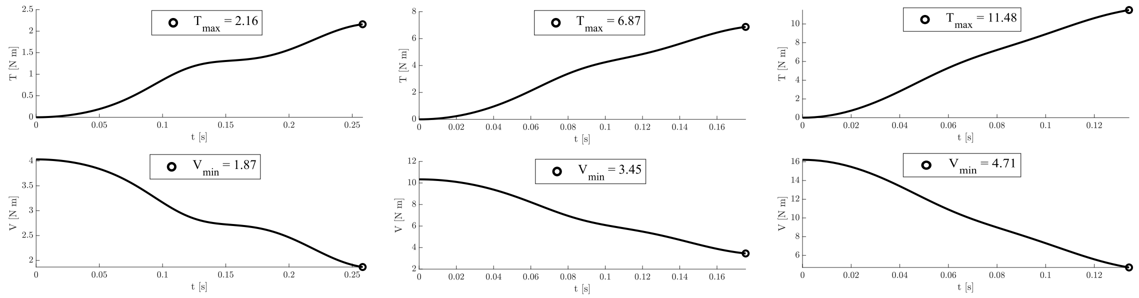

(a) Shell 1 (b) Shell 2 (c) Shell 3

Fig. 20. Total kinetic T and potential energy V at t_{blos}.

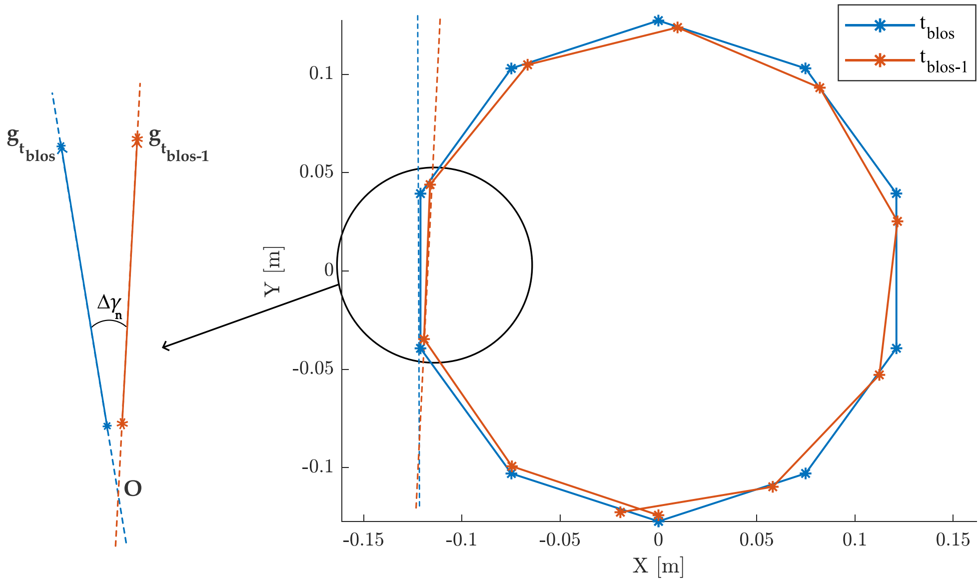

Fig. 21. Shell's discretisation with $n = 10$ homogeneous bars at t_{blos} and t_{blos-1} to geometrically calculate the initial speed $\dot{\theta}_{n_i}$ of each n-bar.

between the lines is given by Eq. (16).

$$\dot{\theta}_{n_i} = \frac{\Delta\gamma}{\Delta t} \tag{15}$$

$$\Delta\gamma_{n_i} = tan^{-1}\left|\frac{g_{t_{blos-1}} - g_{t_{blos}}}{1 + g_{t_{blos}} g_{t_{blos-1}}}\right| \tag{16}$$

5.1.2. Model dynamics

Given the model's initial conditions, the deployment process is carried out by changing the angle of each bar θ_n until the equilibrium positions are reached, which implies until the shell is fully deployed. The Lagrange's Equations, presented in Eq. (3), are used to resolve the equations of motion, where the generalised coordinates of the system q_i are the angles θ_n and the non-conservative generalised forces Q_i are the dissipative forces D generated by the n dampers included in the multi-pendulum system. The damping coefficient c is tuned based on the deployment time comparison with testing and it is the same for all the shells given the common matrix material. Fig. 22 shows a schematic representation of the multi-pendulum model, where m and l_b are the mass and uniform length of the bars and G_n is the centre of mass of each bar. Gravity g is also included in the model.

To describe the dynamics of the multi-pendulum model of Fig. 22 with the Lagrangian $\mathcal{L} = T - V$, the total kinetic and potential energy and the dissipative force acting on the system are evaluated and generalised for n bars with Eqs. (17), (18) and (19), respectively as:

$$T = \frac{1}{2}m\sum_{i=1}^{n}\sum_{j=1}^{n}\left(\frac{l_b^2}{4}\dot{\theta}_i^{\,2} + (n-i)\,l_b^2\dot{\theta}_i^{\,2} + \sigma_{ij}l_b^2\dot{\theta}_i\dot{\theta}_j\cos\left(\theta_j - \theta_i\right)\right) + \frac{1}{2}J\sum_{i=1}^{n}\dot{\theta}_i^{\,2} \tag{17}$$

$$V = \frac{1}{2}\left(k_1\theta_1^2 + \sum_{i=1}^{n-1}k_{i+1}\left(\theta_{i+1} - \theta_i\right)^2\right) - mg\sum_{i=1}^{n}\left(\frac{l_b}{2}\sin(\theta_i) + (n-i)\,l_b\sin(\theta_i)\right) \tag{18}$$

$$D = \frac{1}{2}c\left(\dot{\theta}_1^2 + \sum_{i=1}^{n-1}\left(\dot{\theta}_{i+1} - \dot{\theta}_i\right)^2\right) \tag{19}$$

where J is the moment of inertia of each rigid bar about its center of mass and σ_{ij} is a step function defined as:

$$\sigma_{ij} = \begin{cases} 0, & \text{if } j \le i, \\ p, & \text{if } i < j \le n, \text{ with } p = \overline{p}(1+z). \end{cases} \tag{20}$$

where the values p are given by the position $z+1$ of a vector $\overline{p}$, defined as $\overline{p}$ = [1:2:2n-3] and the variable z is defined as $z = n - j$ and varies between $0 \le z \le n - 2$.

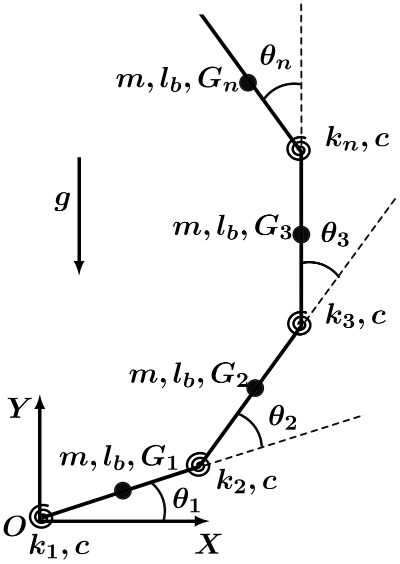

Fig. 22. Multi-pendulum model.

5.1.3. *Stiffness variation function*

The stiffness variation that occurs during deployment is implemented by changing the stiffness of the rotational springs at each time step. Such a variation is built by defining a stiffness function based on the angle of each pendulum. Analogous to the moment–rotation relationship presented in Seffen and Pellegrino (1999), the stiffness function is built between a high and a low value of the stiffness, which are calculated from the shell's moment–rotation relationship and the shell's initial conditions. The smallest value of the stiffness function is defined by Eq. (13). At this condition, the shell is flat and curved, and its state of stiffness is the lowest. For all the shells, such a value was calculated for the three shell's states identified by changing some material properties and friction data, as shown in Figs. 15(a), 16(a) and 17(a). The highest stiffness value, at which the shell recovers its transverse curvature, is estimated by considering the gradient of the initial part of the moment–rotation curve. From such a curve, the angles at which the stiffness becomes non-linear are also taken as references to build the stiffness function. The curve was obtained by conducting a FE simulation in which a longer shell was bent by applying equal-sense moments to the reference points built on the neutral axis of the cross-section, as in Shore et al. (2022). A Riks step was used to assess the non-linear moment–rotation curve, which is shown for each shell in Fig. 23. For Shell 1, the angles at which the low and high stiffness gradients were calculated are highlighted with dashed lines and a yellow and orange point on the curves, respectively. For Shell 2 and 3, the low stiffness gradients were calculated once the curves suitably plateaued. This part of the curves and the low stiffness gradients location are not represented graphically.

The stiffness function values are summarised in Table 4. Based on the local variation on the springs' stiffness as a function of θ, the function allows the pendulum system's stiffness to globally and smoothly vary between the minimum and maximum values. In fact, as the deployment starts, the shell gradually recovers its stiffness along the longitudinal direction from the tip and close to the root, where the shell is constrained, to the central part after forming the final hinge, as shown in Fig. 19. The high stiffness value was considered the same for all the shell's states, given that it was found to not significantly impact the solution. In fact, in order to highlight the stiffness function features used to derive the speed solutions, in Figs. 24(a) and 24(b), the baseline low and high value of the stiffness function reported in Table 4 for Shell 1, (i.e., $k_{low} = 0.686\ \mathrm{N\,m^{-1}}$ and $k_{high} = 429.41\ \mathrm{N\,m^{-1}}$), were increased and reduced of 20%, respectively.

Table 3
Blossoming tip's speed and time from testing and analytical model.

		v [m s^{-1}]			t [s]		
		EXP	Model $\pm^{max}_{min}$	%	EXP	Model $\pm^{min}_{max}$	%
Shell 1	Test 1	5.128		9.1	0.256		0.78
	Test 2	4.68	$4.661 \pm^{4.80}_{4.334}$	0.41	0.26	$0.258 \pm^{0.247}_{0.269}$	0.77
	Test 3	4.861		4.11	0.267		3.37
Shell 2	Test 1	6.949		3.03	0.176		0.57
	Test 2	6.703	$6.738 \pm^{7.08}_{6.444}$	0.51	0.178	$0.175 \pm^{0.166}_{0.184}$	1.69
	Test 3	7.07		4.69	0.184		4.89
Shell 3	Test 1	8.435		4.82	0.149		4.7
	Test 2	8.393	$8.028 \pm^{8.325}_{7.575}$	4.34	0.155	$0.142 \pm^{0.136}_{0.148}$	8.39
	Test 3	7.516		6.37	0.150		5.33

Table 4
Stiffness function values based on the moment–rotation relationship.

		k_{high}		k_{low}	
Shell 1	$\boldsymbol{k}$ [N m^{-1}]	429.41	429.41	$0.686 \pm^{0.695}_{0.675}$	$0.686 \pm^{0.695}_{0.675}$
	$\boldsymbol{\theta}$ [°]	0	0.212	0.233	360
Shell 2	$\boldsymbol{k}$ [N m^{-1}]	867.54	867.54	$1.267\pm^{1.294}_{1.239}$	$1.267\pm^{1.294}_{1.239}$
	$\boldsymbol{\theta}$ [°]	0	0.225	0.237	360
Shell 3	$\boldsymbol{k}$ [N m^{-1}]	1220.2	1220.2	$1.73\pm^{1.795}_{1.684}$	$1.73\pm^{1.795}_{1.684}$
	$\boldsymbol{\theta}$ [°]	0	0.251	0.266	360

The results showed that by changing the low stiffness value, it had a greater impact on the speed solution than changing the high stiffness value. In fact, in Fig. 24(a) it can be seen that by increasing the low stiffness value the speed predictions are higher and the second speed peak occurs faster (blue curve). Whereas coherently, by reducing the low stiffness value, the shell has less driving energy to deploy, resulting in lower and slower speed predictions (black curve). This suggests that the changes or variations in the laminates mechanical properties have a noticeable effect on the deployment dynamics, given that the cross-section is flat when the shell is in the low stiffness regime. Therefore, less stiffness is derived from the geometry, and the material properties play a more dominating role. In contrast, varying the high stiffness value shows to have less effect on the maximum speed and deployment time, as illustrated in Fig. 24(b).

5.2. *Results and discussion*

To describe the multi-pendulum motion and assess the tip's speed, the shell's structure was split into a finite number of bars and the initial conditions of the system were set through Eqs. (13)–(16) and Table 4. Given the small initial radius of $r = 0.05\,\mathrm{m}$ for Shell 1 and 2 and $r = 0.06\,\mathrm{m}$ for Shell 3, $n = 40$ was considered sufficiently fine to shape a circle for all the designs. Secondly, Eqs. (17)–(19), were derived to resolve the n-equations of motion in MATLAB. At t_{blos}, the multi-pendulum system initiated the deployment through the variation of the bars' angles and the change of the elastic strain energy occurring in the rotational springs. Taking Shell 2 as the representative sample data with $k_{low} = 1.267\ \mathrm{N\ m^{-1}}$, Fig. 25 illustrates the multi-pendulum motion from t_{blos} until $t = 0.73\,\mathrm{s}$ when the shell is fully deployed. It can be seen that, as the deployment starts, the major bar angle change occurs at the tip, causing the shell's tip to stiffen rapidly by straightening the last bars. Whereas, close to the root the angle variation is small such that the bars maintain their initial low stiffness feature. Because the shell is still flexible in this region, it forms a hinge that, during the deployment, moves along the longitudinal direction until it disappears after the shell entirely recovers the structural stiffness. The different stages of the deployment path are well captured by the multi-pendulum model and are compared to the test video frames in Figs. 26 to 29. It can be seen that the multi-pendulum model predicts the transition from the closed shell's "C" shape in Fig. 26 to the open "L" shape in Fig. 28, before extending completely.

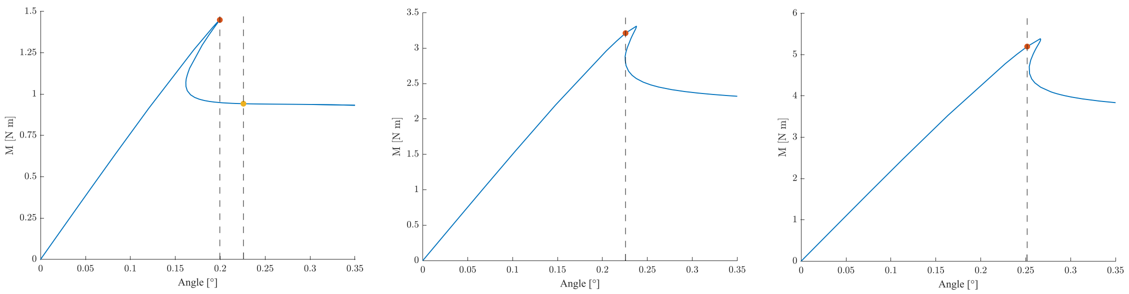

(a) Shell 1 (b) Shell 2 (c) Shell 3

Fig. 23. Moment–rotation relationship obtained from the FE simulations. The orange points represent the high stiffness gradient values. The yellow point in (a) is the low stiffness gradient value for Shell 1.

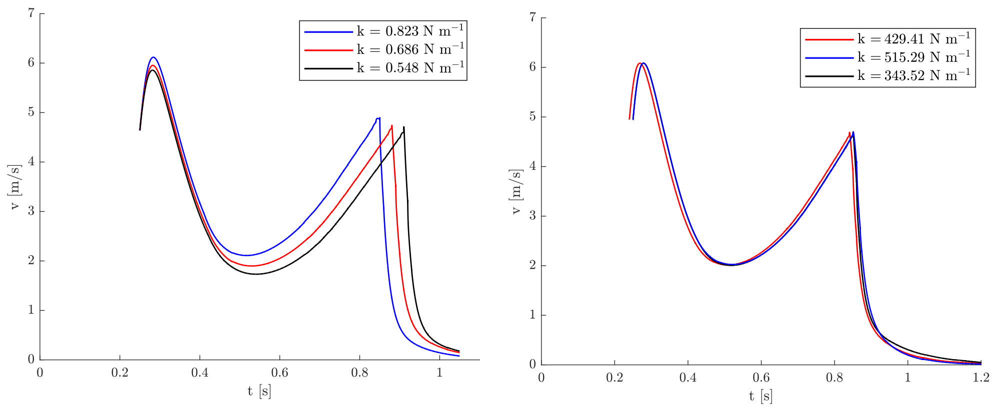

(a) Low stiffness value variation. (b) High stiffness value variation.

Fig. 24. Multi-pendulum speed's result for Shell 1.

Observing the test video frames, it can be seen that the hinge develops at a distance that is further from the root than the distance $d = 0.2$ m that is identified at t_{blos}, as shown in Fig. 26. In fact, as the deployment started, the shell slightly translated, offsetting the hinge from the root due to the increased ploy length. When compared to the multi-pendulum model solutions, it can be seen that the hinge is closer to the root and less pronounced than the test when it reaches the tip, as shown in Fig. 29. This is due to an assumed lower stiffness value at the root in the multi-pendulum model given that, as mentioned in Section 4.3, the clamped part of the shell's root and the ploy region were neglected in this study. In fact, the elastic strain energy of this section, which is highlighted in blue from −0.2 m to 0 m, was not considered in the multi-pendulum model since the root was merged to the ploy region into a single constrained point at 0 m. Although the translation of the hinge was not encouraged by the ploy length's extension, it can be seen to move in Fig. 28 and increase in Fig. 29.

Along with the motion path that developed after t_{blos}, the multi-pendulum model provided the estimations of the tip speed of the system for the three shells. These velocities were derived for the baseline configuration and the lower and upper bound limits defined in Section 4.3 by varying some mechanical properties and friction values. These results were then compared to the test results, which were enclosed in an area of solutions. This comparison is shown in Figs. 30(a)–30(c) for Shell 1, 2 and 3, respectively.

Concerning the analytical velocities, it can be observed a general trend of the curves in which two peaks were identified in proximity to the initial and the final phase of the deployment. For all the shells, the first peak occurred right after t_{blos}, when the shell opens into the "C" shape, as illustrated in Fig. 26. The final peak instead developed when the hinge approached the tip, causing the shell to snap from curved to flat in the last stage of the deployment, as shown in Fig. 29. This peak occurred after a valley of the curve where the shell slowed down before accelerating again. After the last peak, the speed dropped sharply as the shell returned to its deployed state.

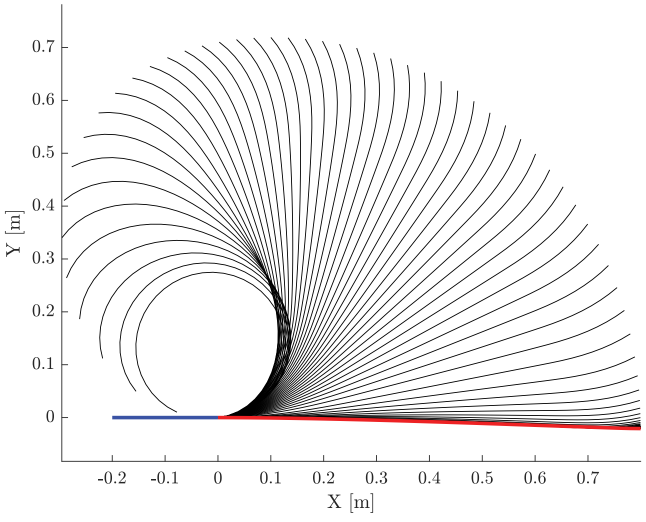

Fig. 25. Multi-pendulum motion. The blue line highlights the ploy region. The red line shows the deployed shell.

Looking at the test results, the valley in which the speed plateaued around a stable value was captured for Shell 1 between $t = 0.31$ s and $t = 0.76$ s. In these time frames, the hinge that formed after t_{blos} remained at the same distance from the root without translating while the shell's tip was forming the "L" shape. This translation is also visible in Figs. 27 and 28 for Shell 2. However, the valley that formed in

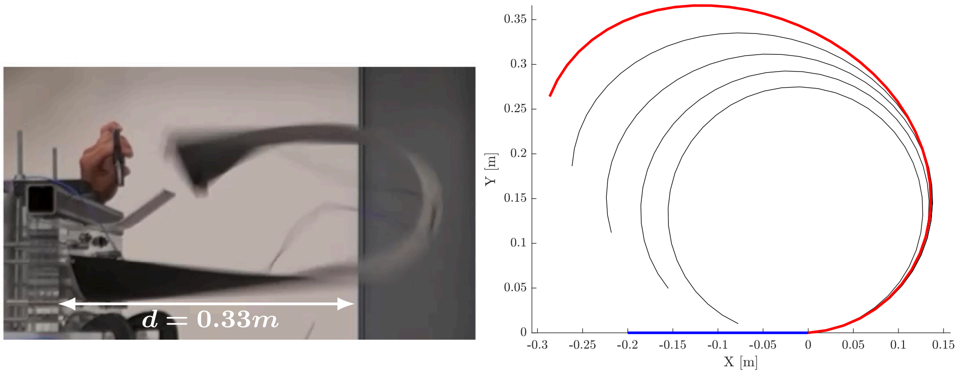

Fig. 26. Shell 2 analytical tip path at $t = 0.22$ s compared to test at $t = 0.24$ s.

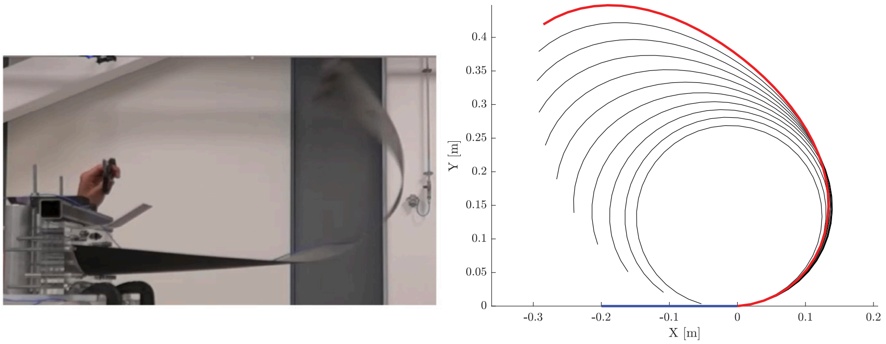

Fig. 27. Shell 2 analytical tip path at $t = 0.35$ s compared to test at $t = 0.36$ s.

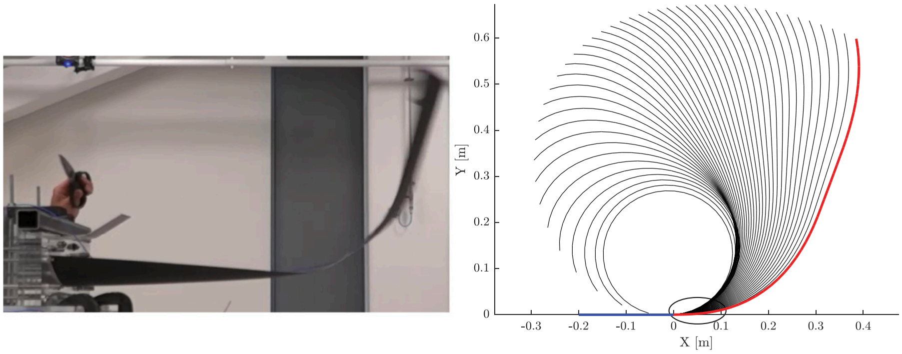

Fig. 28. Shell 2 analytical tip path at $t = 0.43$ s compared to test at $t = 0.44$ s.

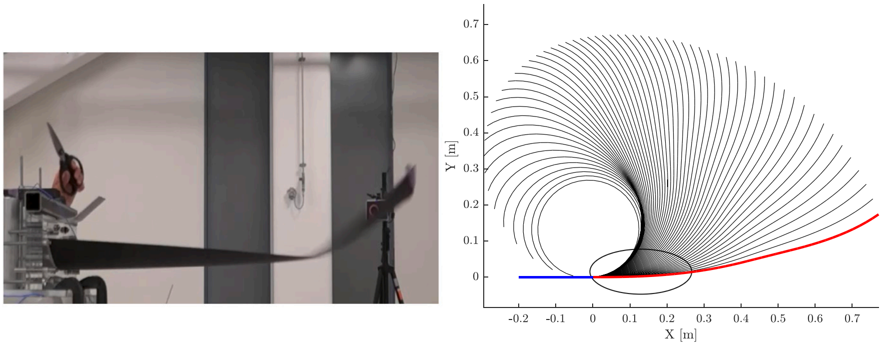

Fig. 29. Shell 2 analytical tip path at $t = 0.56$ s compared to test at $t = 0.57$ s.

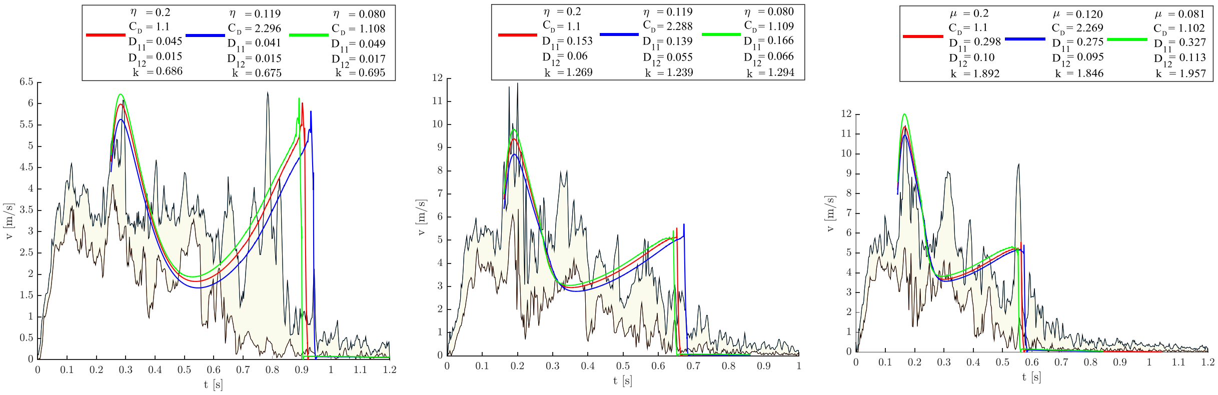

(a) Shell 1 (b) Shell 2 (c) Shell 3

Fig. 30. Multi-pendulum speed's result compared to area of tests' solutions.

Table 5
Multi-pendulum tip's deployment time compared to testing.

		EXP [s]	Model [s]	%
Shell 1	1st peak	0.29	$0.282\ \pm^{0.280}_{0.284}$	2.76
	2nd peak	0.783	$0.902\ \pm^{0.89}_{0.931}$	13.1
	End	0.98	$0.941\ \pm^{0.91}_{0.96}$	3.98
Shell 2	1st peak	0.2	$0.192\ \pm^{0.191}_{0.196}$	4
	2nd peak	0.571	$0.652\ \pm^{0.642}_{0.663}$	12.5
	End	0.73	$0.678\ \pm^{0.665}_{0.712}$	7.12
Shell 3	1st peak	0.168	$0.166\ \pm^{0.167}_{0.168}$	1.19
	2nd peak	0.555	$0.552\ \pm^{0.556}_{0.562}$	0.54
	End	0.68	$0.611\ \pm^{0.559}_{0.605}$	10.1

Shell 2 and 3 is less defined. In these cases, an oscillatory behaviour occurred after the first peak such that another peak was identified at approximately $t = 0.35$ s. At this time, it was observed that the more rigid shells twisted while deploying, causing the tip to move rapidly in the out-of-plane direction. This condition is not captured by the multi-pendulum model as the model is two-dimensional.

Generally, it can be seen that the time at which the initial and final peaks occurred is in good correlation with testing. The maximum speed is also qualitatively in good agreement with the maximum values resulting from the area of tests' solutions, thus proving that the two models were well connected. This is true especially for the first peak provided that the damping value was tuned to trace the maximum value of the speed and the total deployment time. Due to a more chaotic behaviour of the shell's tip after the first peak, the speed and deployment time difference slightly increased in the prediction of the second peak, although the total deployment time is captured well. The difficulty in predicting the second peak is also related to the impact that the variation of the material properties has on the shell's stiffness. As shown in Fig. 24, by changing the low stiffness value due to the implementation of different mechanical properties, the speed results are affected by delaying or moving up the shell's final snapping. Unlike the high stiffness value, that is a stronger function of the geometry, the low stiffness value actively depends on the material. Therefore, small imperfections in the initial geometry do not significantly affect the deployment dynamics; rather, the mechanical properties govern the low stiffness structural regime. The comparison of the peaks' time occurrence for the three shells is presented in Table 5.

By comparing the different shells' behaviour, it can be seen that, in agreement with testing, the stiffer shells, Shell 2 and Shell 3, deploy faster than Shell 1. This is due to a higher initial kinetic energy resulting from the final conditions at t_{blos} which is also shown in Fig. 20. The multi-pendulum model also predicts well the increased values of the speed at the corresponding first peak times for Shell 2 and Shell 3 that, due to higher stiffness properties, exhibit a higher deployment speed than the thinner shell, Shell 1.

6. Conclusion

The DERCA-SAR technology was introduced to investigate the deployment dynamics of different designs of a HSC shallow shell coiled at a radius smaller than the natural radius $r < R$ and then released by exploiting the elastic strain energy stored during stowage. Two analytical models were proposed to predict the deployment speed at the tip and simulate two subsequent deployment phases identified through testing. First, an expanding circle model was presented to describe blossoming and was resolved with a Lagrangian approach. The approximated spiral path resulting from testing was predicted by implementing a convective reference frame that changed the system coordinates based on the test set-up configuration. The path trend and number of turns were well predicted. However, the analytical path was more uniform than the test paths, which were "stretched" in the horizontal direction due to the presence of the ploy region, which was neglected in the model. With less than 10% difference for Shell 1, 5% and 7% for Shells 2 and 3, the analytical tip's velocities were in good agreement with testing. By varying some material properties, the results showed that bending stiffness had the most significant effect on the speed solution, and gravity had an energetic effect that increased the deployment speed and produced an oscillatory trend. The speed predictions followed the test data very well in the initial blossoming and captured the testing change of concavity in the final part. A very good correspondence in the blossoming time resulted for Shell 1 with 0.8% and for Shell 2 with 0.6% difference with Test 1. For Shell 3 such a difference became more relevant showing that the stiffer the shell was, the more it translated during blossoming. The analytical model did not accurately predict this due to underestimating the total strain energy and neglecting the ploy region. Coherently with the test data, the results showed an increase in the deployment speed and a reduction in the deployment time as the shell thickness increased. The speed and time resulted in 4.661 m s^{-1} and 0.258 s for Shell 1, 6.738 m s^{-1} and 0.175 s for Shell 2 and 8.028 m s^{-1} and 0.142 s for Shell 3.

The second analytical model consisted of a Hencky-type model (Wang et al., 2020c) that discretised the shell's structure in a multi-pendulum system and was implemented to capture the more complex dynamics. Such a system was connected by elastic rotational hinges/springs and dampers, and the stiffness-changing behaviour that the shell underwent after t_{blos} was modelled by implementing a stiffness function. The non-linear change of the stiffness enabled the change of the shell's shape from "C" to "L" and the occurrence of a natural hinge that travelled along the shell's longitudinal direction during deployment. The system's dynamics were resolved with Lagrange's equations that were built with the proposed generalised energy equations in Eqs. (17)–(19). The results showed that the multi-pendulum model predicted the shell's motion well by instantly changing the bars' angles at the tip while maintaining a low stiffness close to the root. This formed a hinge at the root, as it was observed during testing. However, given that the ploy region was neglected in the model, differently from the test, such a hinge did not offset from the root as the deployment started, rather it disappeared as the shell approached the final deployment phase before snapping. Despite this, the curves of the tip's velocities highlighted two main peaks that were in good correlation with the initial and final peak given by testing. In fact, the time at which the first peak occurred differed from the test results by 2.76%, 4% and 1.19% for Shell 1, 2 and 3, respectively. Whereas the difference slightly increased for the final peak due to less accuracy of the multi-pendulum model in simulating the uncontrolled and more chaotic behaviour of the tip in the final snap. The difficulty in predicting the final peak was also due to the impact that the low stiffness value variation had on the results. The results showed that small changes in the mechanical properties of the laminate affect the deployment dynamics by delaying or moving up the shell's final snap. Conversely, it was shown that potential small changes in the initial geometry have a negligible effect on the deployment dynamics, as the shell's high stiffness property is a stronger function of the curved geometry.

CRediT authorship contribution statement

Annalisa Tresoldi: Writing – original draft, Methodology, Investigation, Formal analysis, Conceptualization. **Jason Shore:** Writing – review & editing, Methodology, Conceptualization. **Alfonso Pagani:** Writing – review & editing, Validation. **Guglielmo Aglietti:** Supervision.

Declaration of competing interest

The authors declare that they have no known competing financial interests or personal relationships that could have appeared to influence the work reported in this paper.

Acknowledgment

This research has been funded by the New Zealand Tertiary Education Commission through the Grant 9074-5000824.

Data availability

Data will be made available on request.

References

Aglietti, G., Honeth, M., Gensemer, S., Diegel, O., 2020. Deployable optics for cubesats. In: 33rd Annual Conference on Small Satellites, Utah. https://digitalcommons.usu.edu/smallsat/2020/all2020/135/ no.SSC20-VI-06.

Akbar, P.R., Saito, H., Zhang, M., Hirokawa, J., Ando, M., 2016. Parallel-plate slot array antenna for deployable SAR antenna onboard small satellite. IEEE Trans. Antennas and Propagation 64 (5), 1661–1671. http://dx.doi.org/10.1109/TAP.2016.2536164.

Alotaibi, J.G., Alajmi, A.E., Mehoub, G.A., Yousif, B.F., 2021. Epoxy and polyester composites' characteristics under tribological loading conditions. Polymers 13 (14), https://www.mdpi.com/2073-4360/13/14/2230.

Aziz, E., Chassapis, C., Esche, S., Dai, S., Xu, S., Jia, R., 2008. Online wind tunnel laboratory. In: Proceedings of ASEE Annual Conference and Exposition. ASEE Conferences, https://peer.asee.org/3402.

Barrett, R., Taylor, R., Keller, P., Codell, D., Adams, L., 2007. Deployable reflectors for small satellites. In: 21st AIAA/USU. https://api.semanticscholar.org/CorpusID:43591810.

Birk, R., Camus, W., Valenti, E., McCandless, W., 1995. Synthetic aperture radar imaging systems. IEEE Aerosp. Electron. Syst. Mag. 10 (11), 15–23. http://dx.doi.org/10.1109/62.473408.

Brinkmeyer, A., Pellegrino, S., Weaver, P.M., 2015. Effects of long-term stowage on the deployment of bistable tape springs. J. Appl. Mech. 83 (1), http://dx.doi.org/10.1115/1.4031618.

Calladine, C., 1983. Theory of Shell Structures. Cambridge University Press, http://dx.doi.org/10.1017/CBO9780511624278.

Chahat, N., Decrossas, E., Gonzalez-Ovejero, D., Yurduseven, O., Radway, M.J., Hodges, R.E., Estabrook, P., Baker, J.D., Bell, D.J., Cwik, T.A., Chattopadhyay, G., 2019. Advanced CubeSat antennas for deep space and earth science missions: A review. IEEE Antennas Propag. Mag. 61 (5), 37–46. http://dx.doi.org/10.1109/MAP.2019.2932608.

Davis, B., Turse, D., Francis, W.H., 2019. The deployment of large de-orbit sails utilizing high strain composite booms. In: AIAA 2019-1750. http://dx.doi.org/10.2514/6.2019-1750.

Fernandez, J.M., 2017. Advanced deployable shell-based composite booms for small satellite structural applications including solar sails. In: International Symposium on Solar Sailing. https://ntrs.nasa.gov/api/citations/20170001569/downloads/20170001569.pdf.

Fernandez, J.M., Visagie, L., Schenk, M., Stohlman, O.R., Aglietti, G.S., Lappas, V.J., Erb, S., 2014. Design and development of a gossamer sail system for deorbiting in low earth orbit. Acta Astronaut. 103, 204–225. http://dx.doi.org/10.1016/j.actaastro.2014.06.018.

Filippazzo, G., Dinand, S., 2017. The potential impact of small satellite radar constellations on traditional space systems. In: ISAE SUPAERO.

Filippi, M., Carrera, E., 2017. Dynamic analyses of axisymmetric rotors through three-dimensional approaches and high-fidelity beam theories. J. Vib. Acoust. 139 (6), 061008. http://dx.doi.org/10.1115/1.4036927.

Hetzler, H., 2009. On moving continua with contacts and sliding friction: Modeling, general properties and examples. Int. J. Solids Struct. 46 (13), 2556–2570. http://dx.doi.org/10.1016/j.ijsolstr.2009.01.037.

Hoskin, A., Viquerat, A., Aglietti, G.S., 2017. Tip force during blossoming of coiled deployable booms. Int. J. Solids Struct. 118–119, 58–69. http://dx.doi.org/10.1016/j.ijsolstr.2017.04.023.

Huang, J., 2007. Reflectarray antennas. In: Companies, T.M.-H. (Ed.), Antenna Engineering Handbook. https://www.accessengineeringlibrary.com/content/book/9780071475747.

Kim, Y., Jordan, R.L., 2006. Spaceborne SAR antennas for earth science. In: Book, W.A.I. (Ed.), Spaceborne Antennas for Planetary Exploration. http://dx.doi.org/10.1002/0470052783.ch6.

Kirchägner, B., 2016. Finite elements in rotordynamics. Proc. Eng. Int. Conf. Vibr. Prob. 2015 144, 736–750. http://dx.doi.org/10.1016/j.proeng.2016.05.079.

Lee, A., Fernandez, J.M., 2018. Mechanics of bistable two-shelled composite booms. In: AIAA Spacecraft Structures Conference. http://dx.doi.org/10.2514/6.2018-0938, https://arc.aiaa.org/doi/abs/10.2514/6.2018-0938.

Mao, H., Shipsha, A., Tibert, G., 2017. Design and Analysis of Laminates for Self-Deployment of Viscoelastic Bistable Tape Springs After Long-Term Stowage. J. Appl. Mech. 84 (7), 071004. http://dx.doi.org/10.1115/1.4036672.

Okuizumi, N., Katsumata, N., Natori, M.C., Yamakawa, H., 2014. Stepwise deployment of membrane space structures with rolled-up booms: Experiments and simulations. In: Spacecraft Structures Conference. http://dx.doi.org/10.2514/6.2014-1039, https://arc.aiaa.org/doi/abs/10.2514/6.2014-1039.

Pagani, A., Augello, R., Carrera, E., 2023. Numerical simulation of deployable ultra-thin composite shell structures for space applications and comparison with experiments. Mech. Adv. Mater. Struct. 30 (8), 1591–1603. http://dx.doi.org/10.1080/15376494.2022.2037173.

Peral, E., Im, E., Wye, L., Lee, S., Tanelli, S., Rahmat-Samii, Y., Horst, S., Hoffman, J., Yun, S.-H., Imken, T., Hawkins, D., 2018. Radar technologies for earth remote sensing from CubeSat platforms. In: Proceeding of the IEEE. 106, pp. 404–418. http://dx.doi.org/10.1109/JPROC.2018.2793179, 3.

Rimrott, F.P.J., Fritzsche, G., 2000. Fundamentals of STEM mechanics. In: Pellegrino, S., Guest, S.D. (Eds.), IUTAM-IASS Symposium on Deployable Structures: Theory and Applications. Springer Netherlands, Dordrecht, pp. 321–333. http://dx.doi.org/10.1007/978-94-015-9514-8_34.

Seefeldt, P., Spietz, P., Spröwitz, T., 2014. The preliminary design of the GOSSAMER-1 solar sail membrane and manufacturing strategies. In: Macdonald, M. (Ed.), Advances in Solar Sailing. Springer Berlin Heidelberg, Berlin, Heidelberg, pp. 133–151. http://dx.doi.org/10.1007/978-3-642-34907-2_10.

Seffen, K.A., Pellegrino, S., 1999. Deployment dynamics of tape springs.. Proc. R. Soc. Lond. A 455, 1003–1048. http://dx.doi.org/10.1098/rspa.1999.0347.

Shore, J., Viquerat, A., Richardson, G., Aglietti, G., 2022. The bending of thin strips with a non-uniform transverse curvature. Int. J. Solids Struct. 259, 112026. http://dx.doi.org/10.1016/j.ijsolstr.2022.112026, URL https://www.sciencedirect.com/science/article/pii/S0020768322004796.

Subramaniam, N., R., B., Sinha, F.D., Blum, Y.-R.C., Dharani, L.R., 1991. Glass fiber based friction materials. Int. J. Polym. Mater. Polym. Biomater. 15 (2), 93–102. http://dx.doi.org/10.1080/00914039108031526.

Tresoldi, A., Mencarelli, S., Shore, J., Yotov, V., Austin, A.C., Aglietti, G., Ploy region study of a high-strain composite rolled-up deployable shell for a nanosatellite SAR antenna. In: AIAA SCITECH 2023 Forum. http://dx.doi.org/10.2514/6.2023-1702, https://arc.aiaa.org/doi/abs/10.2514/6.2023-1702.

Tresoldi, A., Shore, J., Austin, A.C.M., Aglietti, G.S., 2023a. Deployer design and testing of a deployable rolled-up composite sar antenna DERAC-SAR for cubesats. In: 16th European Conference on Spacecrafts Structures Materials and Environmental Testing. ECSSMET.

Tresoldi, A., Shore, J., Austin, A.C., Aglietti, G.S., 2023b. Development of a deployable synthetic aperture radar antenna for a nanosatellite conceptual design. Acta Astronaut. 210, 488–497. http://dx.doi.org/10.1016/j.actaastro.2023.04.009.

Turse, D., Adams, L., Medina, K.A., Steele, K., Stern, T., 2019. Design, analysis and testing of a composite beam roll-out array (COBRA) for small satellites. In: AIAA 2019-2024. http://dx.doi.org/10.2514/6.2019-2024.

Wang, S., Schenk, M., Guo, H., Viquerat, A., 2020a. Tip force and pressure distribution analysis of a deployable boom during blossoming. Int. J. Solids Struct. 193–194, 141–151. http://dx.doi.org/10.1016/j.ijsolstr.2020.01.026.

Wang, S., Schenk, M., Jiang, S., Viquerat, A., 2020b. Blossoming analysis of composite deployable booms. Thin-Walled Struct. 157, 107098. http://dx.doi.org/10.1016/j.tws.2020.107098.

Wang, B., Seffen, K., Guest, S., 2019. Folding of Bistable Composite Tape-Springs. Tech. Rep., University of Cambridge, http://dx.doi.org/10.17863/CAM.36403, (CUED/D-STRUCT/TR.252).

Wang, S., Xu, S., Lu, L., Sun, L., 2024. Driving force and blossoming analysis of a composite triangular rollable and collapsible (TRAC) boom used in aerospace technologies. Aerospace 11 (4), https://www.mdpi.com/2226-4310/11/4/311.

Wang, C.M., Zhang, H., Challamel, N., Pan, W.H., 2020c. Hencky Bar-Chain/Net for Structural Analysis. WORLD SCIENTIFIC (EUROPE), http://dx.doi.org/10.1142/q0237, https://www.worldscientific.com/doi/abs/10.1142/q0237.

Xue, Y., Li, Y., Guang, J., Zhang, X., Guo, J., 2008. Small satellite remote sensing and applications – history, current and future. Int. J. Remote Sens. 29 (15), 4339–4372. http://dx.doi.org/10.1080/01431160801914945.

Yang, L., Tan, H., Cao, Z., 2018. Modeling and analysis of the ploy region of bistable composite cylindrical shells. Composite Structures 192, 347–354. http://dx.doi.org/10.1016/j.compstruct.2018.02.085.

Yeong-Bae, K., Sung, J.G., Hyuk, l.J., 2023. Numerical and experimental investigation of the deployment stability of bistable composite tape springs. Available at SSRN http://dx.doi.org/10.2139/ssrn.4439684.

Zhang, X., Li, K.-Z., Li, H.-J., Fu, Y.-W., Fei, J., 2014. Tribological and mechanical properties of glass fiber reinforced paper-based composite friction material. Tribol. Int. 69, 156–167. http://dx.doi.org/10.1016/j.triboint.2013.08.003.

Zhi-Quan, L., Hui, Q., Li, X., Yang, S.-L., 2017. Review of large spacecraft deployable membrane antenna structures. Chin. J. Mech. Eng. 30, 1447–1459. http://dx.doi.org/10.1007/s10033-017-0198-x.